The Astrophysical Journal, 736:37 (27pp), 2011 July 20 doi:10.1088/0004-637X/736/1/37

SUBMILLIMETER ARRAY/PLATEAU DE BURE INTERFEROMETER MULTIPLE LINE OBSERVATIONS OF THE NEARBY SEYFERT 2 GALAXY NGC 1068: SHOCK-RELATED GAS KINEMATICS AND HEATING IN THE CENTRAL 100 pc?*

M. Krips[1], S. Martín[2], A. Eckart[3], R. Neri[1], S. García-Burillo[4], S. Matsushita[5,6], A. Peck[6,7], I. Stoklasová[8], G. Petitpas[9], A. Usero[4], F. Combes[10], E. Schinnerer[11], L. Humphreys[12], and A. J. Baker[13]
[1] Institut de Radio Astronomie Millimétrique, 300 Rue de la Piscine, Domaine Universitaire, F-38406 Saint Martin d'Hères, France; krips@iram.fr, neri@iram.fr
[2] European Southern Observatory, Alonso de Córdova 3107, Vitacura, Casilla 19001, 19 Santiago, Chile; smartin@eso.org
[3] I. Physikalisches Institut, Universität zu Köln, Zülpicher Str. 77, 50937 Köln, Germany; eckart@ph1.uni-koeln.de
[4] Observatorio Astronómico Nacional (OAN)-Observatorio de Madrid, C/Alfonso XII 3, 28014 Madrid, Spain; s.gburillo@oan.es, a.usero@oan.es
[5] Institute of Astronomy and Astrophysics, Academia Sinica, P.O. Box 23-141, 10617 Taipei, Taiwan; satoki@asiaa.sinica.edu.tw
[6] Joint ALMA Office, Joint ALMA Observatory, Alonso de Córdova 3107, Vitacura, Casilla, 19001, 19 Santiago, Chile; apeck@alma.cl
[7] NRAO, 520 Edgemont Road, Charlottesville, VA 22903, USA
[8] Astronomical Institute of the Academy of Sciences of the Czech Republic, v.v.i., Boční II 1401, 14131 Prague, Czech Republic
[9] Harvard-Smithsonian Center for Astrophysics, SMA Project, 60 Garden Street MS 78, Cambridge, MA 02138, USA; gpetitpa@cfa.harvard.edu
[10] Observatoire de Paris, LERMA, 61 Avenue de l'Observatoire, 75014 Paris, France; francoise.combes@obspm.fr
[11] Max-Planck-Institut für Astronomie, Königstuhl 17, 69117 Heidelberg, Germany; schinner@mpia.de
[12] ESO, Karl-Schwarzschild-Strasse 2, D-85748 Garching, Germany; ehumphre@eso.org
[13] Department of Physics and Astronomy, Rutgers, The State University of New Jersey, 136 Frelinghuysen Road, Piscataway, NJ 08854-8019, USA; ajbaker@physics.rutgers.edu
Received 2011 February 22; accepted 2011 May 6; published 2011 July 1

ABSTRACT

We present high angular resolution (0″.5–2″.0) observations of the millimeter continuum and the ^{12}CO(J = 3–2), ^{13}CO(J = 3–2), ^{13}CO(J = 2–1), C^{18}O(J = 2–1), HCN(J = 3–2), HCO$^+$(J = 4–3), and HCO$^+$(J = 3–2) line emission in the circumnuclear disk ($r \lesssim 100$ pc) of the prototypical Seyfert 2 galaxy NGC 1068, carried out with the Submillimeter Array. We also include in our analysis new ^{13}CO(J = 1–0) and improved ^{12}CO(J = 2–1) observations of NGC 1068 at high angular resolution (1″.0–2″.0) and sensitivity, conducted with the Institute de Radioastronomie Millimetrique Plateau de Bure Interferometer. Based on the complex dynamics of the molecular gas emission indicating non-circular motions in the central ∼100 pc, we propose a scenario in which part of the molecular gas in the circumnuclear disk of NGC 1068 is blown radially outward as a result of shocks. This shock scenario is further supported by quite warm ($T_{\rm kin} \geqslant 200$ K) and dense ($n({\rm H_2}) \simeq 10^4$ cm^{-3}) gas constrained from observed molecular line ratios. The HCN abundance in the circumnuclear disk is found to be [HCN]/[^{12}CO] ≈ $10^{-3.5}$. This is slightly higher than the abundances derived for Galactic and extragalactic star-forming/starbursting regions. This result lends further support to X-ray-enhanced HCN formation in the circumnuclear disk of NGC 1068 as suggested by earlier studies. The HCO$^+$ abundance ([HCO$^+$]/[^{12}CO] ≈ 10^{-5}) appears to be somewhat lower than that of Galactic and extragalactic star-forming/starbursting regions. When trying to fit the centimeter-to-millimeter continuum emission by different thermal and non-thermal processes, it appears that electron-scattered synchrotron emission yields the best results while thermal free–free emission seems to overpredict the millimeter continuum emission.

Key words: galaxies: active – galaxies: individual (NGC 1068) – galaxies: ISM – galaxies: kinematics and dynamics – galaxies: nuclei – galaxies: Seyfert – radio continuum: galaxies – radio lines: galaxies – submillimeter: galaxies

Online-only material: color figures

1. INTRODUCTION

Little is known about the effects of active processes in galaxies on the chemical and kinematic properties of the surrounding molecular gas and vice versa, whether the activity is in the form of an active galactic nucleus (AGN) or a starburst (SB), or both. Information on the characteristics of the molecular gas in the vicinity of the activity is essential to reveal the underlying physical processes because molecular gas constitutes a large fraction of the fuel for the central activity and thus helps to keep it alive over cosmologically relevant timescales. Also, the feedback of activity into the surrounding molecular gas represents an important factor for the evolution of the activity (with respect to outflows or shocks, for instance). The large diversity and often also simultaneity of the physical processes accompanying the different activity types certainly complicate any interpretation of the interaction between the activity and the molecular gas. These processes include large-scale shocks, gas outflow and inflow, other dynamical perturbations, and strong radiation fields, such as through UV or X-ray radiation, cosmic rays, or supernovae explosions (e.g., Martín et al. 2011; García-Burillo et al. 2010; Sakamoto et al. 2010; Papadopoulos 2010; Pérez-Beaupuits et al. 2009; Krips et al. 2008; Aalto 2008; Matsushita et al. 2007; García-Burillo et al. 2007; Martín et al. 2006; Usero et al. 2006; Sakamoto et al. 2006; Matsushita et al. 2005; Fuente et al. 2005; Meier & Turner 2005; Usero et al. 2004). Thus, a thorough study of the kinematics, excitation conditions, and chemistry of the molecular gas close to AGNs and SBs is essential for understanding the nature and evolution of these active environments.

* Based on observations carried out with the IRAM Plateau de Bure Interferometer. IRAM is supported by INSU/CNRS (France), MPG (Germany), and IGN (Spain).

Table 1
Properties of NGC 1068

Characteristic	NGC 1068	Reference
Hubble class	(R)SA(rs)b	NED[a]
AGN type	Seyfert 2	Khachikian & Weedman (1974)
Dynamical center	$\alpha_{J2000} = 02^h42^m40\overset{s}{.}70$	Gallimore et al. (2004)
	$\delta_{J2000} = -00°00'47\overset{''}{.}9$	
Redshift	0.00379 ± 0.00001	Huchra et al. (1999)
Systemic velocity	(1137 ± 3) km s^{-1}	Huchra et al. (1999)
Luminosity distance	12.6 Mpc[b]	NED[a]
Scale	61 pc arcsec^{-1}	NED[a,b]
Inclination angle	40°	Bland-Hawthorn et al. (1997)
Position angle	278°	Bland-Hawthorn et al. (1997)

Notes.
[a] NED: NASA/IPAC Extragalactic Database.
[b] Used cosmology: Hubble constant $H_0 = 73$ km s^{-1}Mpc^{-1}, Omega(matter) = 0.27, and Omega(vacuum) = 0.73.

High angular resolution observations of ^{12}CO emission, a reliable tracer of the global molecular gas reservoir, are an important step to study the dynamics in active galaxies. ^{12}CO alone, however, certainly cannot describe the complexity of the molecular gas close to the activity processes (especially with respect to the chemistry and excitation conditions of the molecular gas). Moreover, ^{12}CO has been found to be an unreliable tracer of dense molecular gas environments (at least its lower rotational transitions), in which most AGN- or star-formation activity is supposed to take place (e.g., Krips et al. 2007; Gao & Solomon 2004). Observations at high angular resolution of different molecular tracers are thus a next logical step. Given recent upgrades of current (sub)millimeter interferometers, the detection and spatial resolution of weaker molecular lines become feasible tasks.

In this paper, we present high angular resolution observations of the (sub)millimeter continuum and ^{12}CO, ^{13}CO, C^{18}O, HCN, and HCO$^+$ line emission in the nearby Seyfert 2 galaxy NGC 1068, conducted with the Submillimeter Array (SMA) and the Institute de Radioastronomie Millimetrique Plateau de Bure Interferometer (PdBI).

2. NGC 1068

The nearby Seyfert 2 galaxy NGC 1068 (see Table 1 for a general overview) has not only become the figurehead for the viewing angle unification theory for Seyfert galaxies (e.g., Krolik & Kallman 1987), but also its center most impressively exhibits the characteristics for harboring an obscured Seyfert 1 AGN (Antonucci & Miller 1985). It has also become a prime example of the significantly different effects that an AGN can have on the excitation conditions and chemistry of the surrounding molecular gas when compared to an SB or quiescent galaxies (e.g., Krips et al. 2008; Usero et al. 2004; Kohno et al. 2001; Sternberg et al. 1994). The prototypical nature of NGC 1068 is certainly due in part to its relatively small distance from Earth (12.6 Mpc) and its strong continuum as well as line emission from X-ray and radio frequencies, making it an ideal target to study the accretion and feedback processes of its AGN in unprecedented detail. As a (fortunate) consequence, a wealth of information is already available for this source, the most relevant of which will be summarized in this section.

The molecular gas in NGC 1068 is distributed in an SB ring/spiral ∼3 kpc (∼50″) in diameter, a stellar bar ∼2 kpc (∼30″) in length, and a circumnuclear disk/ring (CND) ∼200 pc (∼3″) in diameter (e.g., Schinnerer et al. 2000, and references therein). At the very center of the CND, pronounced H_20 maser emission suggests a thin disk of a few parsec in diameter (e.g., Gallimore et al. 2001; Greenhill et al. 1996). A pronounced jet and counterjet can be observed from centimeter to millimeter wavelengths (e.g., Krips et al. 2006; Gallimore et al. 2004) that extend from the maser disk out to several kiloparsecs from the center. Mid-IR (MIR) observations reveal hot and ionized gas that biconically follows the path of the radio jet (e.g., Müller-Sànchez et al. 2009; Poncelet et al. 2008; Tomono et al. 2006; Galliano et al. 2005; Bock et al. 2000) and indicates the existence of a parsec-scale warm dust torus (Jaffe et al. 2004). Early high angular resolution radio-continuum observations indicated an interaction of the radio jet with the neighboring interstellar medium (ISM) due to the apparently disrupted structure of the (northern) jet (radio components NE and C in, e.g., Gallimore et al. 1996; Roy et al. 1998). However, in a later publication, Gallimore et al. (2004) argue that the observed disturbed jet structure (in NE) can also be explained by variable outflow speeds due to variable accretion (e.g., Gallimore et al. 2001; Siemiginowska & Elvis 1997), though an earlier collision at position C was not discarded.

The complex dynamics of the molecular gas as traced by the ^{12}CO(2–1) line emission within the CND were interpreted as a consequence of a warped disk (Schinnerer et al. 2000). However, more recent observations of the MIR rovibrational H_2 emission have started to raise doubts about this interpretation (e.g., Müller-Sànchez et al. 2009) and alternatively suggest that the complex gas kinematics are due to a funneling of the gas toward the AGN along the jet (the inner 60 pc) plus an expanding ring (on a scale of $r = 100$–150 pc), the latter having been already proposed a few years before by Galliano & Alloin (2002).

Additional fascinating characteristics of the CND of NGC 1068, besides the complex kinematic behavior of its molecular gas, are its chemistry and excitation conditions, which appear to significantly differ from SB/star-forming environments. Traced by the "abnormal" line ratios of different molecules and transitions, mostly by HCN, HCO$^+$, and ^{12}CO, it has been suggested that the CND in NGC 1068 harbors a giant X-ray-dominated region (XDR; e.g., Kohno et al. 2008; Usero et al. 2004; Tacconi et al. 1994; Sternberg et al. 1994). XDRs are defined in a similar way to the photon-dominated regions (PDRs) in SB galaxies (such as M82; e.g., Fuente et al. 2005) but are driven by X-ray rather than UV radiation. High HCN-to-CO($J = 1$–0) ($\geqslant$1) and HCN-to-HCO$^+$($J = 1$–0) ($\geqslant$1) ratios are found in the CND of NGC 1068, indicating enhanced HCN abundances there. The X-ray radiation of the AGN is therefore supposed to be the main driver for the enhancement of HCN. It can penetrate much deeper into the surrounding molecular gas than the UV radiation in PDRs, leading to a stimulated "hyper"-production of HCN. A multi-transition, multi-molecular line study of HCN and HCO$^+$ conducted with the IRAM 30 m telescope (Krips et al. 2008) supports an increased abundance of HCN and/or increased kinetic temperatures. Both can explain equally the elevated HCN-to-^{12}CO(1–0) line ratios either by the aforementioned enhancement of the HCN abundance and/or a hypo-excitation of the low J^{12}CO transitions (see also M51 and NGC 6951 as examples of increased HCN/^{12}CO($J = 1$–0) ratios; Krips et al. 2009, 2007; Matsushita et al. 2007, 2004; Kohno et al. 1996).

Recent SiO interferometric observations of the CND in NGC 1068 carried out by García-Burillo et al. (2010) testify further to the complexity of the gas chemistry in this galaxy. The

Table 2
Chronological Summary of Observations Carried Out for NGC 1068

Molecular Line	Telescope	Observing Dates (YYYY-MM)	Config.[a]	Frequency at Rest (GHz)	Band	Zenith Opacity at 225 GHz	T_{sys} (K)	rms Noise[b] (mJy)	Synthesized Beam Major×Minor, P.A.[c] (″×″,°)
^{13}CO($J=2$–1) & C^{18}O($J=2$–1)	SMA	2008-01, 2008-02	EX	220.399 219.560	LSB LSB	0.10–0.20	100–150	12	1.0 × 0.8,30[d]
HCO$^+$($J=4$–3)	SMA	2007-08, 2007-09	EX	356.734	USB	0.06–0.13	200–400	32[e]	1.0 × 0.8,30[f]
^{12}CO($J=3$–2)	SMA	2007-09	EX	345.796	LSB	0.06–0.13	200–400	51	1.0 × 0.8,30[f]
HCO$^+$($J=3$–2)	SMA	2006-11	EX	267.558	LSB	0.06–0.15	100–150	33	1.0 × 0.8,30[f]
HCN($J=3$–2)	SMA	2006-01	EX	265.886	LSB	0.05–0.10	100–150	24[e]	1.0 × 0.8,30[e,f]
	SMA	2006-10, 2006-11	VEX		LSB	0.10–0.22	100–200		0.53 × 0.46,30[d,e]
^{13}CO($J=3$–2)	SMA	2005-10	C	356.734	USB	0.05–0.06	200–300	39	2.4 × 2.1,28[d]
^{13}CO($J=1$–0)	PdBI	2003-02	A	110.201	SSB	n.a.	150–300	1.7	2.5 × 1.9,28[f]
^{12}CO($J=2$–1)	PdBI	2003-02	A	230.538	SSB	n.a.	200–600	4	1.0 × 0.8,30[e]

Notes.
[a] SMA configurations: C = compact (baselines up to 70 m); EX = extended (baselines up to 220 m); VEX = very extended (baselines up to 500 m); PdBI configurations: A = most extended (baselines up to 500 m).
[b] In 17 km s^{-1} wide channels.
[c] P.A. is measured from north to east.
[d] Using uniform weighting.
[e] Combined for all tracks.
[f] Using natural weighting.

bright SiO emission in its CND suggests an enhanced abundance of this molecule, which is interpreted by the authors as closely related to (high-velocity) shocks. The shocks are believed to be a consequence of a jet–gas interaction.

3. OBSERVATIONS

A summary of all (sub)millimeter interferometric observations is given in Table 2, where observing parameters as well as achieved rms noise and angular resolutions are listed.

3.1. SMA

For all SMA observations, unless otherwise stated, the phase reference center has been set to α_{J2000} =02^{h}42^{m}40^s.70 and δ_{J2000} =−00°00′47″.9, which corresponds to the radio position of the active nucleus (e.g., Gallimore et al. 2004; Krips et al. 2006). The SMA receivers have been tuned to the respective lines using Doppler tracking of the systemic velocity of NGC 1068, $v_{LSR} = 1137$ km s^{-1}. Both the upper sideband (USB) and lower sideband (LSB) were used for the observations, yielding a bandwidth of 2 GHz each, separated by 10 GHz. A spectral resolution of 0.81 MHz was used for all observations, corresponding to 0.8 km s^{-1} at 1 mm. The 225 GHz zenith opacity τ_{225} was measured regularly throughout all observations at the nearby Caltech Submillimeter Observatory. The accuracy of the flux calibration for all tracks is estimated to be at a conservative level of ∼20%.

The SMA data have been reduced with SMA-specific tasks in the MIR package (Scoville et al. 1993). Further image analysis has been conducted with the GILDAS package (Guilloteau & Lucas 2000).

3.1.1. HCN($J = 3$–2) Emission

We observed the HCN($J = 3$–2) line emission in NGC 1068 using the extended and very extended configurations with up to eight 6 m dishes in 2006 January, October, and November. The 345 GHz receivers were tuned to the HCN($J = 3$–2) line (265.886 GHz at rest) in the LSB; the USB was used for continuum measurements. The weather conditions were good with opacities of $\tau_{225} = 0.05$–0.1 in the January track (extended configuration) and $\tau_{225} = 0.13$–0.22 in the October and November tracks (very extended configuration). We used 3C273, 3C111, and/or 3C454.3 as bandpasses and Uranus, Titan, and/or Neptune as flux calibrators.[14] We observed two quasars (0235+164, 0238−084, 0339−017, and/or 0423−013) every ∼15 minutes to calibrate the gains (amplitude and phase versus time). The data from all three tracks were combined into a single data file, resulting in an rms noise of 24 mJy in 17 km s^{-1} wide velocity channel. The synthesized beam was determined to be 1″.0 × 0″.8 at a position angle of P.A. = 30° (natural weighting) and 0″.53 × 0″.46 at P.A. = 30° (robust weighting).

3.1.2. HCO$^+$($J = 3$–2) Emission

We carried out observations of the HCO$^+$($J = 3$–2) emission in NGC 1068 using seven antennas in extended configuration during 2006 November. The 345 GHz receivers were tuned to the HCO$^+$(3–2) line (267.558 GHz at rest) in the LSB; the USB was used for continuum measurements. The weather conditions were good with opacities of $\tau_{225} = 0.06$–0.15. Bandpass calibrations were performed on 3C273, Titan, and Uranus, while absolute fluxes were determined using Titan. The gains were calibrated on 0423−013 and 0339−017. For this data set, we reached an rms noise of 33 mJy in 17 km s^{-1} wide velocity channels. The synthesized beam was determined to be 1″.0 × 0″.8 at P.A. = 30° (natural weighting).

3.1.3. ^{12}CO($J = 3$–2) and HCO$^+$($J = 4$–3) Emission

The ^{12}CO($J = 3$–2) emission of NGC 1068 was observed in extended configuration using all eight antennas during 2007 September. In addition, the HCO$^+$($J = 4$–3) emission was observed in a separate track in 2007 August. The 345 GHz receivers were tuned to the ^{12}CO($J = 3$–2) line (345.796 GHz at rest) in the LSB such that the HCO$^+$($J = 4$–3) line (356.734 GHz at rest) still fell within the USB. The opacities ranged between

[14] We used the line-free USB for Titan and Neptune to determine the absolute flux level, as they are known to have broad HCN lines that could contaminate a flux calibration in the LSB.

$\tau_{225} = 0.06$ and 0.13. Bandpass calibrations were performed on 3C454.3 and Uranus. Uranus was also used for flux calibration. Gains were determined using 0238+166 and 0423−013. An rms noise of 80 mJy was reached in 7 km s^{-1} wide velocity channels. The synthesized beam was determined to be $1''.0 \times 0''.8$ at P.A. = 30° for natural weighting when also using a UV taper to better match the angular resolutions of the other SMA observations. The original (untapered) angular resolution amounted to 0.6 × 0.5 at P.A. = 30°.

3.1.4. ^{13}CO(J = 2–1) and C^{18}O(J = 2–1) Emission

The ^{13}CO(J = 2–1) emission in NGC 1068 was observed in extended configuration using all eight antennas during 2008 January and February. The 230 GHz receivers were tuned to the ^{13}CO(J = 2–1) line (220.399 GHz at rest) in the USB such that the C^{18}O(J = 2–1) line (219.560 GHz at rest), the HC$_3$N(J = 23–22) line (209.230 GHz at rest), and the H32α line (210.502 GHz at rest) still fell within the LSB. However, only ^{13}CO(J = 2–1) and C^{18}O(J = 2–1) line emission was detected. The opacities ranged between τ_{225} = 0.1–0.2. Bandpass calibrations were performed on 0423−013, 3C111, and Titan, while gains were determined using 0339−017 and 0423−013. Titan was also used as a flux calibrator. An rms noise of 12 mJy was reached in 17 km s^{-1} wide velocity channels. The synthesized beam was determined to be $1''.0 \times 0''.9$ at P.A. = 30° for natural weighting when also using a UV taper to better match the angular resolutions of the other SMA observations.

3.1.5. ^{13}CO(J = 3–2) Emission

The ^{13}CO(J = 3–2) emission in NGC 1068 was observed in compact configuration using seven antennas in 2005 October. These observations were part of the observing campaign presented by Humphreys et al. (2005), which aimed to detect extragalactic H$_2$O maser emission at (sub)millimeter wavelengths. The 345 GHz receivers were tuned to the H$_2$O(10(2,9)-9(3,6)) maser line (321.226 GHz at rest) in the LSB such that the ^{13}CO(J = 3–2) line (356.734 GHz at rest) was still located within the USB. The 225 GHz zenith opacity remained stable around 0.05–0.06. Bandpass calibrations were performed on 3C454.3, 3C111, and Uranus. Uranus was also used as a flux calibrator. The gains were determined using 0234+285 and verified against 0215+015 and 0420−014. An rms noise of 61 mJy was reached in 7 km s^{-1} wide velocity channels. The synthesized beam was determined to be $2''.4 \times 2''.1$ at P.A. = 28° (natural weighting).

3.2. IRAM PdBI

3.2.1. ^{12}CO(2–1) and ^{13}CO(J = 1–0) Emission

Observations of the ^{12}CO(2–1) emission in NGC 1068 were carried out with the IRAM PdBI in 2003 February using all six antennas in A configuration. Simultaneously, we observed the ^{13}CO(J = 1–0) using the 3 mm PdBI receivers. The bandpasses were calibrated on NRAO150 and 0420−014 while phase and amplitude calibrations were performed on 0235+164 and 0238−084. A total bandwidth of 580 MHz with a spectral resolution of 1.25 MHz was used. We reach an rms of ∼7 mJy in 7 km s^{-1} wide velocity channels (natural weighting) at 1 mm and of ∼1.9 mJy in 14 km s^{-1} wide velocity channels (natural weighting) at 3 mm. Applying natural weighting in the mapping process, beam sizes were derived to be $1''.0 \times 0''.6$ at P.A. = 36° at 1 mm and $2''.5 \times 1''.7$ at P.A. = 28° at 3 mm. However, to better match the SMA observations we mapped the ^{12}CO(2–1) data with a UV taper, giving an effective angular resolution of $1''.0 \times 0''.8$ at P.A. = 30°. As the UV coverages between the SMA and PdBI data (for the high angular resolution data) were very similar, the usage of a simple UV taper already provided the necessary accuracy to match the restoring beam of the PdBI observations with that of the SMA.

4. RESULTS

4.1. Continuum Emission: From 850 μm to 1.4 mm

The sub(millimeter) continuum emission at the wavelengths presented in this paper was derived from the line-free channels of line observations (Table 2), averaging emission from USB and LSB where possible (for the SMA data; the PdBI data were obtained from single-sideband observations). The continuum emission has also been merged between data sets with very similar observed frequencies (i.e., within ∼10 GHz). Before averaging data from different sidebands and/or observations, it was carefully verified that the absolute flux, position, and structure of the emission in the individual data sets were consistent with each other within calibrational uncertainties of 20% (flux) and $0''.1$ (position) in order to reduce systematic errors.

The continuum emission was clearly detected at all wavelengths at a $\geqslant 5\sigma$ level. To obtain accurate fluxes, positions, and sizes, elliptical Gaussians were fitted to the data in the UV plane, except for the uniformly weighted map of the 1.0 mm continuum emission for which a circular Gaussian was fitted, given its apparently unresolved nature. The results of these fits are listed in Table 3.

The continuum emission at 1.0 mm (derived from natural weighting, hereafter NA), 1.3 mm, and 1.4 mm appear to be consistent with each other in terms of their flux, position, and structure (see Table 3 and Figure 1; see also Krips et al. 2006). All show peak fluxes of around 15–19 mJy beam^{-1} and spatially integrated flux densities of 22–28 mJy, indicating extended emission. Their positions, although self-consistent, are slightly to the north (∼$0''.2$) of the radio position of the AGN (component S1 from Gallimore et al. 2004; marked with a white cross in Figure 1) and that of the uniformly weighted 1.0 mm continuum emission (Figure 1(b); white contours). The shift between the millimeter and centimeter data is larger than the positional uncertainty of $0''.1$ and thus assumed to be real. NGC 1068 is known to have a pronounced radio (and millimeter) jet in a northeast-to-southwest direction, of which the northeastern part exhibits the stronger emission (e.g., Gallimore et al. 2004; Krips et al. 2006). Despite the steep spectral index of the synchrotron emission of the jet, the extended (i.e., >1″) emission from both the jet and the counterjet are still visible at 3 mm (e.g., Krips et al. 2006; Schinnerer et al. 2000) but are significantly fainter or undetected at shorter wavelengths (i.e., $\lesssim$1 mm).

The continuum emission at 1.0 mm (NA), 1.3 mm, and 1.4 mm is a blend of emission associated with the (northeast) radio jet and the AGN itself (S1 in Gallimore et al. 2004) due to the "lower" angular resolution of ∼1″. Due to the higher angular resolution, the 1.0 mm continuum emission of the jet in the uniformly weighted map (Figure 1(b)) is almost entirely resolved, leaving behind only the more compact emission of the AGN. Thus, the centroids of the emission at 1.0 mm (NA), 1.3 mm, and 1.4 mm will naturally shift toward the north, while the 1.0 mm (derived from uniform weighting, hereafter UN) continuum emission should reveal the actual position of the AGN (or at least the base of the jet).

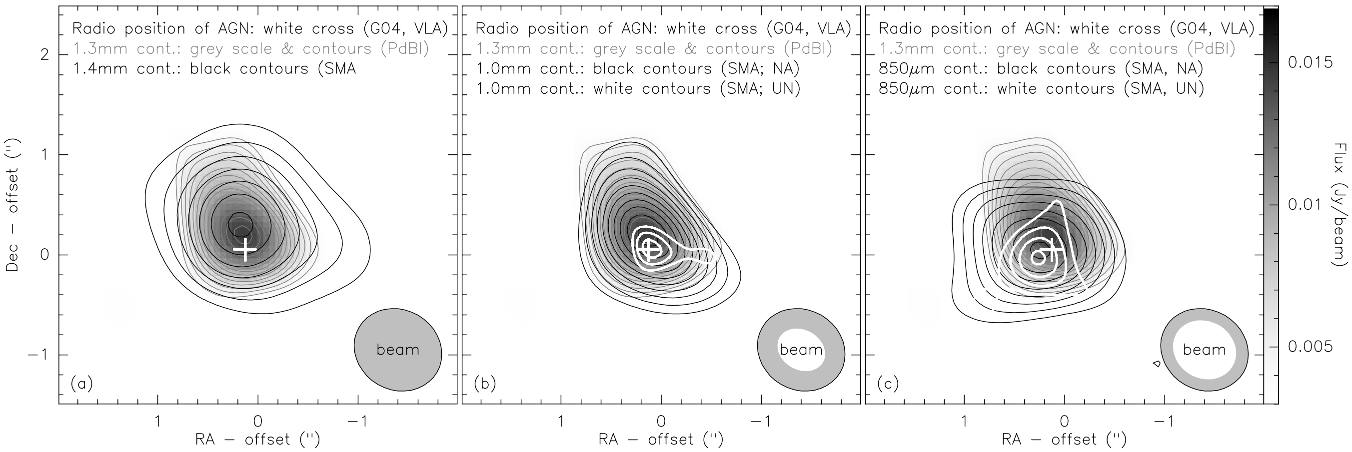

Figure 1. Continuum emission of NGC 1068 at λ = 1.4 mm ((a); black contours), 1.3 mm ((a)–(c); gray scale and gray contours), 1.0 mm ((b); black contours), and 850 μm ((c); black contours), observed with SMA and IRAM PdBI. The white crosses denote the position of the AGN measured by Gallimore et al. (2004, G04). The contours of the 1.3 mm continuum emission (PdBI) start at $5\sigma = 4$ mJy in steps of 1σ. (a) The contours of the 1.4 mm continuum emission (SMA) start at $5\sigma = 4$ mJy in steps of 1σ. (b) The contours of the 1.0 mm continuum emission (SMA, NA) start at $3\sigma = 1.6$ mJy in steps of 1σ, while the contours of the uniformly mapped 1.0 mm continuum emission run from $3\sigma = 2.3$ mJy in steps of 1σ. (c) The contours of the 850 μm continuum emission (SMA, NA) start at $3\sigma = 2.4$ mJy in steps of 1σ, while the contours of the uniformly mapped 850 μm continuum emission run from $3\sigma = 2.6$ mJy in steps of 1σ.

Table 3
Continuum Parameters for NGC 1068

λ	Synth. Beam Major×Minor, P.A. (″×″,°)	$\Delta\alpha$[a] (″)	$\Delta\delta$[a] (″)	Peak Flux (mJy beam^{-1})	Flux Density[b] (mJy)	Deconv. Size Major×Minor, P.A. (″×″,°)
1.4 mm	1.0 × 0.8,30	+0.13 ± 0.02	+0.25 ± 0.02	19 ± 2	28 ± 3	(0.9 ± 0.1) × (0.7 ± 0.1),(50 ± 20)
1.3 mm	1.0 × 0.8,30	+0.18 ± 0.02	+0.23 ± 0.02	15 ± 1	22 ± 2	(0.6 ± 0.1) × (0.5 ± 0.1),(40 ± 20)
1.0 mm (NA)[c]	1.0 × 0.8,30	+0.17 ± 0.05	+0.15 ± 0.10	19 ± 2	24 ± 3	(0.8 ± 0.1) × (0.4 ± 0.1),(20 ± 10)
1.0 mm (UN)[d]	0.5 × 0.4,30	+0.13 ± 0.03	+0.07 ± 0.03	12 ± 2	13 ± 2	(0.3 ± 0.1)[e]
810 μm	2.1 × 2.0,80	−0.04 ± 0.2	−0.07 ± 0.2	30 ± 4	41 ± 11	(1.1 ± 0.1) × (0.8 ± 0.2),(90 ± 20)
850 μm (NA)	1.0 × 0.8,30	+0.33 ± 0.07	+0.05 ± 0.06	24 ± 2	50 ± 7	(1.1 ± 0.1) × (0.8 ± 0.2),(90 ± 20)
850 μm (UN)	0.6 × 0.5,30	+0.33 ± 0.09	−0.03 ± 0.07	16 ± 3	30 ± 5	(1.1 ± 0.1) × (0.8 ± 0.2),(90 ± 20)

Notes.
[a] The offsets are with respect to $\alpha_{J2000} = 02^{h}42^{m}40\overset{s}{.}70$ and $\delta_{J2000} = -00^{\circ}00'47\overset{''}{.}9$, which is almost identical to the radio position of the AGN in NGC 1068 of $\alpha_{J2000} = 02^{h}42^{m}40\overset{s}{.}709$ and $\delta_{J2000} = -00^{\circ}00'47\overset{''}{.}95$ (e.g., Gallimore et al. 2004; Krips et al. 2006). Positional errors are of a pure statistical nature and were derived from the Gaussian fit to the data. They do not include absolute positional uncertainties from the calibration, which are estimated to be $\sim 0\overset{''}{.}1$.
[b] Flux errors are purely statistical and do not account for uncertainties from the flux calibration. Flux calibration uncertainties are estimated to be of the order of 10%–20% (see the text).
[c] Averaged continuum emission derived from the HCN($J = 3$–2) (vex+ext) and HCO^{+}($J = 3$–2) observations (ext). Data were mapped using natural weighting (NA).
[d] Averaged continuum emission derived from the HCN($J = 3$–2) observations alone (vex+ext) using uniform weighting (UN).
[e] Here, only a circular Gaussian fit has been carried out, while for the rest an elliptical Gaussian has been fitted to the data (see the text).

Going to even shorter wavelengths of 850 μm, it appears not only that the continuum flux increases again, but also that its position seems to now be consistent with the AGN, independent of the weighting (i.e., synthesized beam) used for mapping/cleaning, and unlike the 1.0 mm (NA), 1.3 mm, and 1.4 mm continuum emission. The latter may indicate that the emission from the radio jet is negligible at 850 μm (see also Figure 3 in Krips et al. 2006) and the AGN (i.e., the S1 component) dominates. The increased flux at 850 μm, which appears to be larger by almost a factor of two compared to the 1.0−1.4 mm emission, shows that thermal dust emission already plays a significant role at 850 μm (see Section 5.1). Also, the size and shape of the continuum emission appear to have changed compared to those at longer wavelengths. The P.A. of the 850 μm emission ($\sim 90^{\circ}$) is significantly different from that ($\sim 30^{\circ}$) of the 1.0–1.4 mm emission. Moreover, the 850 μm emission appears to be extended (Figure 1(c)), in contrast to the 1.0–1.4 mm emission, which seems to be extended only in the jet component but not in the "leftover" AGN component in the uniformly weighted 1.0 mm map (Figure 1(b)). The uniformly weighted 850 μm continuum emission also appears to be resolved (white contours in Figure 1(c); compare also peak flux density with total flux density in Table 3).

4.2. Line Emission

4.2.1. General Characteristics and Distribution of the Molecular Gas

The continuum emission has been subtracted from all of the line data in the UV plane to avoid any contamination even if in some cases the continuum emission does not exceed the noise level in the individual channel maps (see Tables 2 and 3). In order to reduce systematic effects due to spatial filtering, we used a slight UV taper (giving some more weight to the shorter baselines) to map and clean all line emission data with the same synthesized beam, except for the high angular resolution ($\sim 0\overset{''}{.}4$–$0\overset{''}{.}5$) of the uniformly weighted HCN($J = 3$–2) map (also

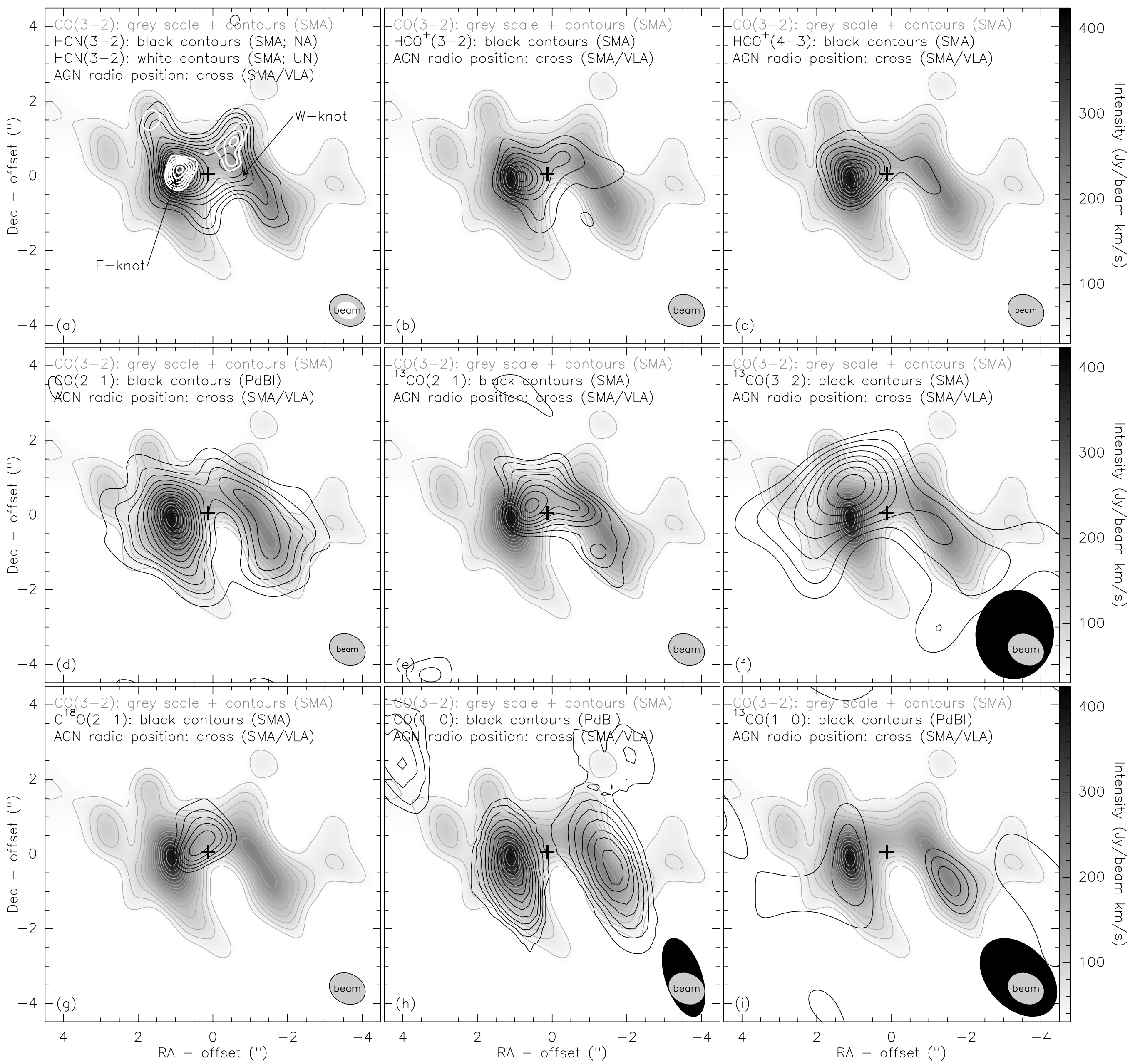

Figure 2. Velocity-integrated line emission of ^{12}CO($J = 3$–2) ((a)–(g)), HCN($J = 3$–2) (a), HCO$^+$($J = 3$–2) (b), HCO$^+$($J = 4$–3) (c), ^{12}CO($J = 2$–1) (d), ^{13}CO($J = 2$–1) (e), ^{13}CO($J = 3$–2) (f), C^{18}O($J = 2$–1) (g), ^{12}CO($J = 1$–0) (h), and ^{13}CO($J = 1$–0) (i) in NGC 1068, observed with SMA and IRAM PdBI. Contour levels are: ^{12}CO($J = 3$–2) from 10σ by 6σ with 1σ = 4.8 Jy km s^{-1}; HCN($J = 3$–2) from 3σ by 1σ with 1σ = 2.6 Jy km s^{-1}; HCO$^+$($J = 3$–2) from 2σ by 1σ with 1σ = 3.4 Jy km s^{-1}; HCO$^+$($J = 4$–3) from 3σ by 1σ with 1σ = 2.4 Jy km s^{-1}; ^{12}CO($J = 2$–1) from 5σ by 5σ with 1σ = 1.2 Jy km s^{-1}; ^{13}CO($J = 2$–1) from 3σ by 1σ with 1σ = 0.9 Jy km s^{-1}; ^{13}CO($J = 3$–2) from 5σ by 1σ with 1σ = 3.5 Jy km s^{-1}; C^{18}O($J = 2$–1) from 3σ by 1σ with 1σ = 0.9 Jy km s^{-1}; ^{12}CO($J = 1$–0) from 5σ by 3σ with 1σ = 0.4 Jy km s^{-1}; ^{13}CO($J = 1$–0) from 1σ by 1σ with 1σ = 0.1 Jy km s^{-1}.

shown in Figure 2(a) using white contours) and the low angular resolution (∼2″) of the ^{12}CO($J = 1$–0), ^{13}CO($J = 1$–0), and ^{13}CO($J = 3$–2) maps.

Figure 2 shows the velocity-integrated intensity maps of the molecular line emission from HCN($J = 3$–2), HCO$^+$($J = 3$–2), HCO$^+$($J = 4$–3), ^{12}CO($J = 2$–1), ^{13}CO($J = 2$–1), ^{13}CO($J = 3$–2), C^{18}O($J = 2$–1), ^{12}CO($J = 1$–0), and ^{13}CO($J = 1$–0); ^{12}CO($J = 3$–2) is plotted in gray scale in all images to facilitate a comparison. All these molecules have been clearly detected above the 5σ level (except ^{13}CO($J = 1$–0)). The emission in all lines reveals a pronounced peak on the stronger eastern knot and, in the stronger lines, also a weaker peak on the western knot, both of which are already known from previous ^{12}CO observations (e.g., Schinnerer et al. 2000). Elliptical Gaussians have been fitted to the UV data for all lines in order to obtain the position, peak, and spatially integrated flux of the emission in the two knots. The results of the fits are given in Table 4. The positions of the emission in the eastern and western knots are very similar in all observed lines, excluding the ^{13}CO($J = 2$–1) and C^{18}O($J = 2$–1) emission which seems to peak closer to the AGN.

The spectrum of the spatially integrated emission (over the central ∼4″) of each line is plotted in Figure 3. We also show the ^{12}CO($J = 1$–0) line emission taken from Schinnerer

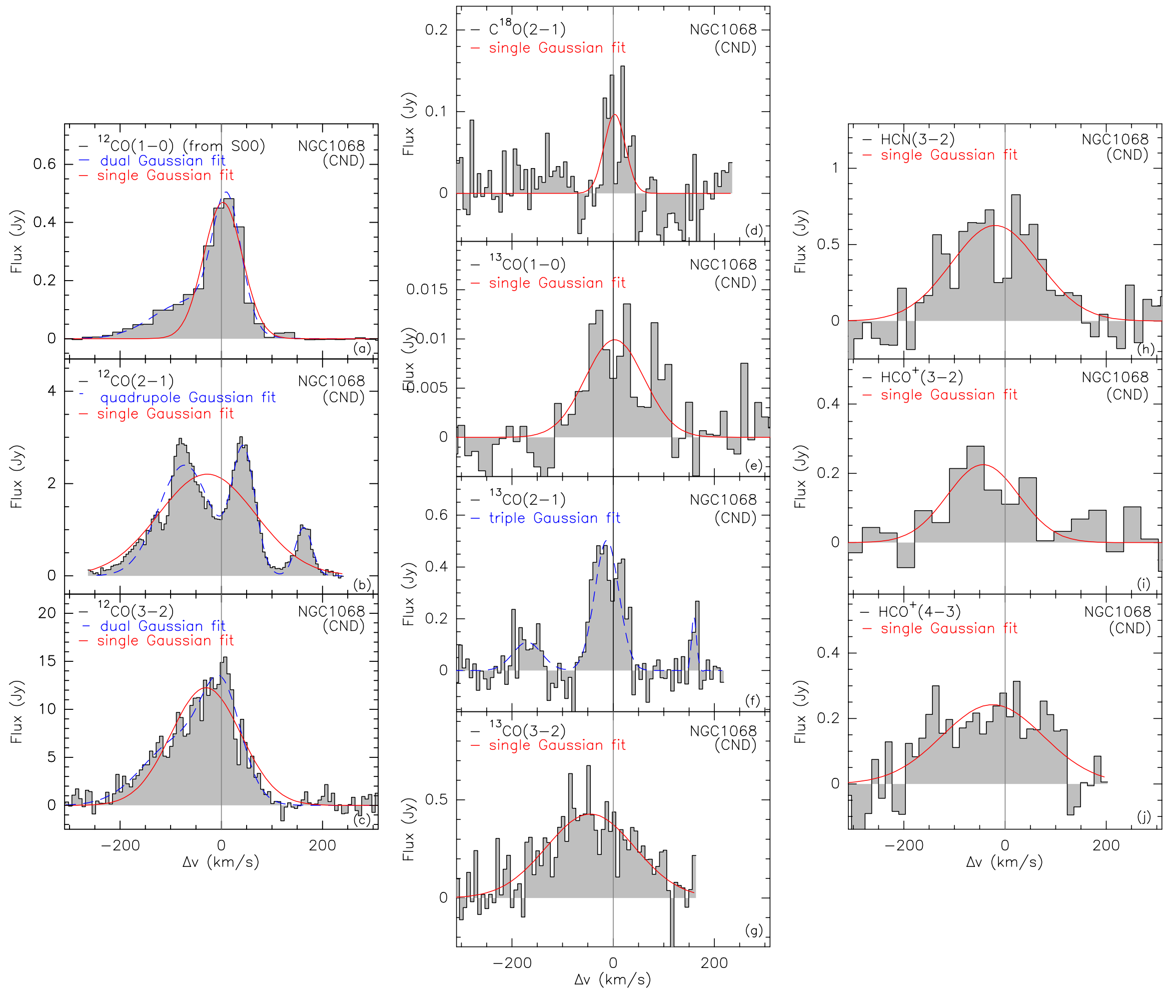

Figure 3. Spatially integrated spectrum of different molecular lines in NGC 1068. The single-line Gaussian fit is indicated with a red dotted line (parameters are listed in Table 5) while the multiple Gaussian fit is plotted with a blue dashed line.

(A color version of this figure is available in the online journal.)

Table 4
Individual Components of the Molecular Line Emission in NGC 1068

Molecular Line	Component	$\Delta\alpha$[a] ($''$)	$\Delta\delta$[a] ($''$)	Vel.-Integrated Peak Intensity[a] (Jy beam^{-1} km s^{-1})	Spatially Integrated Intensity[a] (Jy km s^{-1})
HCN($J = 3$–2)	E-knot	$+1.0 \pm 0.1$	$+0.1 \pm 0.1$	51 ± 8	110 ± 20
	W-knot	-0.8 ± 0.2	$+0.2 \pm 0.2$	32 ± 4	70 ± 10
HCO$^+$($J = 3$–2)	E-knot	$+0.9 \pm 0.1$	$+0.0 \pm 0.1$	28 ± 5	52 ± 5
	W-knot	-0.8 ± 0.2	$+0.5 \pm 0.2$	14 ± 2	40 ± 5
HCO$^+$($J = 4$–3)	E-knot	$+0.9 \pm 0.1$	$+0.1 \pm 0.1$	27 ± 6	98 ± 20
^{12}CO($J = 3$–2)	E-knot	$+1.1 \pm 0.1$	-0.1 ± 0.1	470 ± 20	1330 ± 200
	W-knot	-1.2 ± 0.1	-0.1 ± 0.1	270 ± 10	720 ± 100
^{13}CO($J = 3$–2)	E-knot	$+1.1 \pm 0.1$	$+0.3 \pm 0.1$	24 ± 3	40 ± 10
^{12}CO($J = 2$–1)	E-knot	$+1.0 \pm 0.1$	-0.2 ± 0.1	70 ± 10	290 ± 20
	W-knot	-1.3 ± 0.1	-0.3 ± 0.1	30 ± 5	180 ± 20
^{13}CO($J = 2$–1)	E-knot	$+0.6 \pm 0.2$	$+0.4 \pm 0.2$	10 ± 2	18 ± 3
	W-knot	-1.2 ± 0.3	$+0.1 \pm 0.1$	8 ± 2	16 ± 3
C^{18}O($J = 2$–1)	E-knot	$+0.3 \pm 0.3$	$+0.5 \pm 0.3$	7 ± 1	15 ± 3
^{13}CO($J = 1$–0)	E-knot	$+1.0 \pm 0.4$	-0.4 ± 0.4	0.4 ± 0.2	0.5 ± 0.2
	W-knot	-1.3 ± 0.4	-0.8 ± 0.5	0.4 ± 0.2	0.5 ± 0.2
^{12}CO($J = 1$–0)	E-knot	$+0.5 \pm 0.1$	$+0.1 \pm 0.1$	40 ± 1	90 ± 2
	W-knot	-1.1 ± 0.1	-0.5 ± 0.1	19 ± 1	40 ± 2

Note.
[a] The parameters were determined by fitting a one- or two-component elliptical Gaussian profile to the UV data of each line. Errors include the statistical uncertainties from the Gaussian fit and those from the calibration (∼10%–20%). Offsets are with respect to the center position specified in Table 3.

Table 5
Molecular Line Parameters Derived from the Different Line Spectra of NGC 1068

Molecular Line	Velocity Offset[a,b,c] (km s^{-1})	Line Flux[a] (Jy)	Line Width[a,b,d] (km s^{-1})	Vel.-Integrated Intensity[a,b] (Jy km s^{-1})	Vel.-Integrated SD Intensity[e] (Jy km s^{-1})	SD Beam ($''$)
HCN($J=3$–2)	-30 ± 10	0.63 ± 0.08	200 ± 30	150 ± 10	190 ± 10	9.5
HCO$^+$($J=3$–2)	-40 ± 10	0.23 ± 0.03	190 ± 50	50 ± 6	80 ± 8	9.5
HCO$^+$($J=4$–3)	-40 ± 10	0.24 ± 0.03	240 ± 40	60 ± 6	70 ± 10	14
^{12}CO($J=3$–2)	-30 ± 3	12.3 ± 0.40	170 ± 10	2130 ± 5	2600 ± 300	14
^{13}CO($J=3$–2)	-40 ± 10	0.43 ± 0.03	230 ± 30	100 ± 10	170 ± 20	14
^{12}CO($J=2$–1)	-30 ± 6	2.20 ± 0.10	230 ± 20	529 ± 2	950 ± 6	12
^{13}CO($J=2$–1)	-10 ± 10	0.50 ± 0.04	60 ± 10	30 ± 1	55 ± 7	12
C^{18}O($J=2$–1)	$+3 \pm 10$	0.10 ± 0.02	50 ± 10	5.1 ± 0.3	...	...
^{12}CO($J=1$–0)	$+3 \pm 2$	0.50 ± 0.02	240 ± 10	120 ± 4	650 ± 80	21
^{13}CO($J=1$–0)	$+8 \pm 10$	0.009 ± 0.002	140 ± 30	1.3 ± 0.3	56 ± 7	21

Notes.
[a] The line parameters have been determined by fitting a single Gaussian line to the (spatially integrated) spectrum for each molecule. The line emission has therefore been integrated over the central $4''$ in NGC 1068.
[b] Statistical error from the Gaussian fit only.
[c] With respect to $v_{\rm LSR} = 1137$ km s^{-1}.
[d] FWHM.
[e] Single dish (SD) integrated intensities as measured with the IRAM 30 m and the James Clerk Maxwell Telescope (JCMT) in the central $10''$–$30''$ of NGC 1068 (taken from: Israel 2009; Pérez-Beaupuits et al. 2009; Krips et al. 2008). The values were converted to the Jansky scale using S[Jy]/$T_{\rm mb}$[K] = 4.71 (30 m) and S[Jy]/$T_{\rm mb}$[K] = 15.6 (JCMT).

et al. (2000) for consistency. While the velocity-integrated line emission seems to be very similar in its shape and position for most lines, the line profiles vary significantly from each other. Although for the dense gas tracers (HCN, HCO$^+$) a single Gaussian fit is sufficient to reproduce the line profiles, the CO lines need a dual, triple, or quadrupole Gaussian fit. However, to simplify the comparison, the results given in Table 5 represent a single Gaussian fit to all lines. The line centers are roughly consistent with each other, differing by less than 20 km s^{-1}. Excluding the ^{13}CO($J=2$–1) and C^{18}O($J=2$–1) emission, the line widths also agree with each other within the uncertainties. Except for the ^{12}CO($J=2$–1) and ^{13}CO($J=2$–1) line emission for which roughly half of the emission seems to be resolved, the interferometric observations have captured most of the emission measured with single-dish observations (Table 5). Note that for the ^{12}CO($J=1$–0) (Schinnerer et al. 2000) and ^{13}CO($J=1$–0) emission, the single-dish fluxes are much higher than the interferometric ones because they contain significant emission from the star-forming ring/spiral arms and the bar.

4.2.2. Dynamical Characteristics of the Molecular Gas

The kinematic behavior of the different molecules is presented in detail in Figures 4–11. To better understand the puzzling complexity of the different profiles of the various molecular lines and test whether it is due to dynamical effects, we spatially split the spectra by deriving the spectrum of the western and eastern knots separately (Figure 4). Note that the ^{13}CO($J=1$–0) and C^{18}O($J=2$–1) line emission was discarded because of its insufficient sensitivity and/or lack of emission in the western knot, while the ^{12}CO($J=1$–0) and ^{13}CO($J=3$–2) line emission is not included because of its insufficient angular resolution. The iso-velocity maps (Figure 5) of the ^{12}CO, ^{13}CO, HCN, and HCO$^+$ line emission clearly show a dynamical structure that seems to be dominated by standard disk rotation with a blueshifted eastern knot and a redshifted western knot. If disk rotation were the only underlying kinematics, one would expect to find a simple blueshifted peak at the eastern knot and a redshifted peak at the western knot. Although disk rotation is observed, Figure 4 shows kinematic features significantly differing from simple rotation. Instead, the blueshifted eastern knot also exhibits redshifted emission and the redshifted western knot exhibits blueshifted emission. These "wings" appear to be present in all three lines of ^{12}CO emission at a high significance level, and also appears in the ^{13}CO, HCN and HCO$^+$ emission; however, given the lower signal-to-noise ratio (S/N) for these lines, the wings are not as pronounced as for ^{12}CO. At this point, it should be emphasized that in such a case, the Moment 1 map can be very misleading as it derives only the dominant kinematic structure and might overlook more complex underlying kinematics. Integrating (in velocity) the redshifted and blueshifted parts of the line spectrum (Figure 6) as well as analyzing the channel maps (Figures 7 and 8) might be the more appropriate approach. Figure 6 indicates a more complex distribution than expected from simple disk rotation. We find blueshifted emission spatially coincident with redshifted emission and vice versa; this seems to be most pronounced for the ^{12}CO, ^{13}CO, and HCN emission. By looking at the channel maps of the ^{12}CO($J=2$–1) and ^{12}CO($J=3$–2) emission (which have the highest S/N), the red-on-blueshifted and blue-on-redshifted emission is not only at low velocities but also at higher velocities (which is especially visible in the ^{12}CO($J=2$–1) emission; see channels <-70 km s^{-1} and $>+100$ km s^{-1} in Figure 7). The same is true for the ^{12}CO($J=3$–2) emission (Figure 8; although it is less pronounced, especially for velocities >80 km s^{-1} for which no emission can be found anymore, as opposed to ^{12}CO($J=2$–1)). We find the behavior of the HCN($J=3$–2) emission similar to that of the ^{12}CO($J=2$–1) and ^{12}CO($J=3$–2) emission, though on a much lower significance level. The ^{13}CO($J=2$–1) emission, however, seems to indicate a different behavior (see Figure 9). Instead of being distributed in a "ring"-like manner, the emission appears to be more elongated in a southwest to northeast direction (see especially channel maps between $+50$ km s^{-1} and -20 km s^{-1}). However, given the low sensitivity level, this structure has to be treated with caution and needs

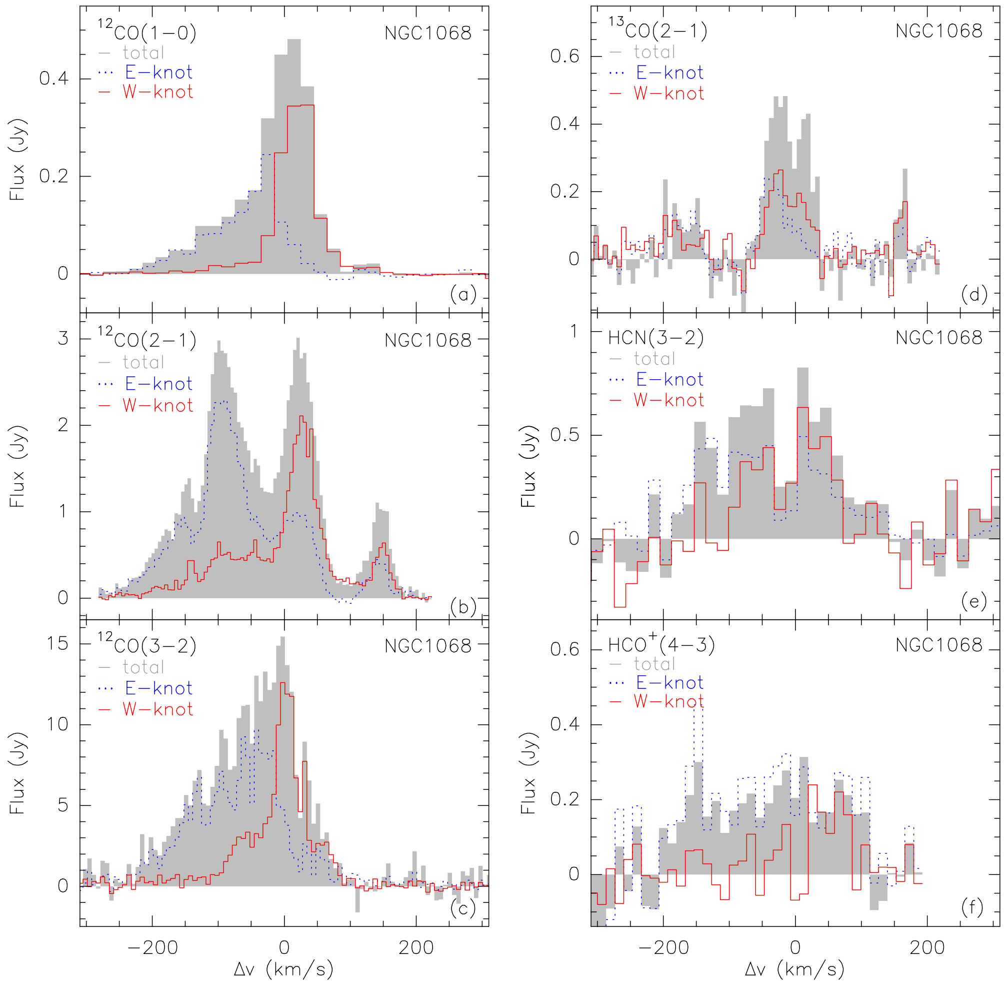

Figure 4. Spatially integrated spectrum of the ^{12}CO(J = 1–0) (taken from Schinnerer et al. 2000), ^{12}CO(J = 2–1) and ^{12}CO(J = 3–2) (left column), and HCN(J = 3–2) and HCO$^+$(J = 4–3) emission over the eastern knot (E-knot; blue dotted line) and western knot (W-knot; red solid line) component of NGC 1068.

(A color version of this figure is available in the online journal.)

confirmation by either higher sensitivity observations or other molecular lines such as SiO. Indeed, the SiO emission seems to indicate a similar behavior as discussed in separate papers (see García-Burillo et al. 2008, 2010).

The position–velocity diagrams of the ^{12}CO and HCN emission, taken at different P.A.s in steps of 30° across the CND, are shown in Figure 10. The gray scale denotes the ^{12}CO(J = 2–1) emission for better comparison. Overall, the kinematic structures in the different lines strongly resemble each other. Also, the overlap of the red-on-blueshifted emission can be seen quite well in the position–velocity diagrams (see especially P.A. = 60°–120° in Figure 10), strongly indicating pronounced non-circular motions in the CND of NGC 1068.

In order to quantify and parameterize the observed complex kinematics, we follow the approach used by Heckman et al. (1989) and Baum et al. (1992). We determine three kinematic parameters from the slits taken at the different P.A.s used in Figure 10 for the ^{12}CO emission. These parameters are: (1) the average line-of-sight velocity dispersion σ, determined as $0.426 \times$ FWHM along each slit, (2) the "rotational" velocities Δ, determined from the difference between the average velocities on either side of the nucleus along each slit, and (3) the rms variation of the velocity ϵ for each point along the slit, defined as $\epsilon = \sqrt{\frac{1}{N}\Sigma_{i=1}^{N}(v_i - v_{\rm av})^2}$, where N is the number of points along the slit, v_i is the intensity-weighted velocity for point i, and $v_{\rm av}$ is the intensity-weighted average velocity along the slit. A comparison of the different parameters with each other, especially the ratios $\frac{\Delta}{\sigma}$ and $\frac{\Delta}{\epsilon}$, allows us to classify the dynamics into three different groups (for a more detailed explanation we refer to Baum et al. 1992):

Rotators: $\Delta/\sigma \gtrsim 1, \Delta/\epsilon \gtrsim 1$

Calm non-rotators: $\Delta/\sigma < 1, \Delta/\epsilon \sim 1$

Violent non-rotators: $\Delta/\sigma < 1, \Delta/\epsilon < 1$.

The results of this kinematic parameterization for the ^{12}CO(J = 2–1) emission are shown in Figure 11, highlighting our previous findings (we find very similar values when analyzing the ^{12}CO(J = 3–2) emission). For most P.A.s, we find that the ratios are most consistent with calm non-rotation with one exception (P.A. = 60°) being located in the area of the violent non-rotators. This strongly emphasizes the fact that although there is an underlying dominating disk rotation, the dynamics of the molecular gas in the CND of NGC 1068 is significantly disturbed by a non-rotational process, most significantly for the north to northeastern part of the CND (i.e., along P.A. = 0°–90°). We also attempted to determine the rotational velocities directly by azimuthally averaging the velocities within the CND and then subsequently fitting rotational curves to the data using `rotcurv`

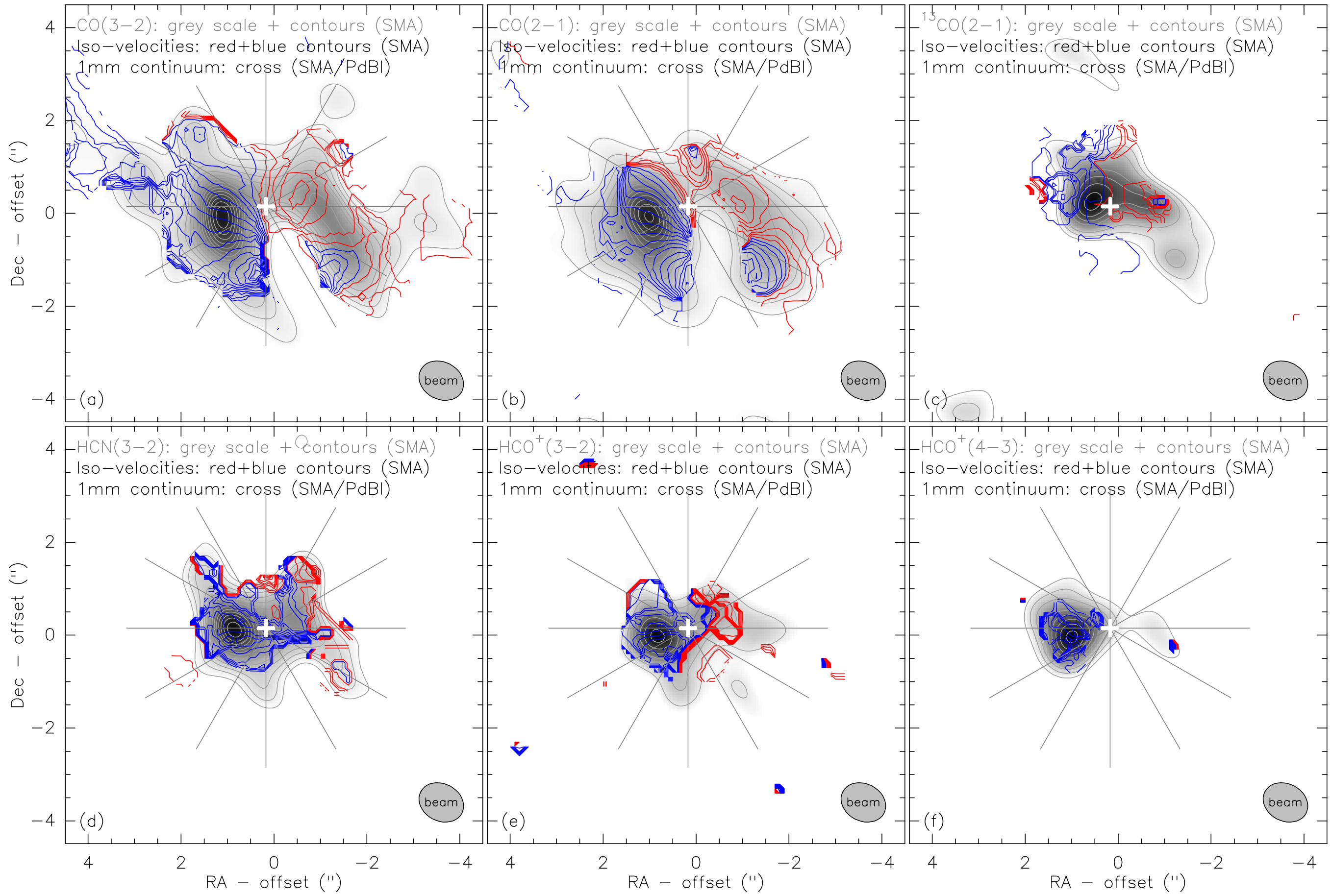

Figure 5. Iso-velocity maps of the different molecular lines observed in NGC 1068. The gray scale corresponds to the velocity-integrated emission of each line with the same contours as used in Figure 2. The velocity contours are in steps of 10 km s^{-1} around the systemic velocity of NGC 1068. The gray lines indicate the cuts along which the position–velocity diagrams (see Figure 10) were taken for the respective molecules (^{12}CO($J = 2$–1),^{12}CO($J = 2$–1), and HCN($J = 3$–2)).

(A color version of this figure is available in the online journal.)

in GIPSY. We then assumed different scenarios ranging from pure disk rotation to adding a radial dependency. However, no physically meaningful result could be obtained. We mostly find positive velocities that decrease with radius, which is inconsistent with simple disk rotation (see also the dynamical analysis done in Schinnerer et al. 2000) and necessitates the inclusion of a bulge or central mass component, whether in the form of a nuclear star cluster or a massive black hole in addition to the disk. This certainly further emphasizes the complexity of the molecular gas dynamics in the CND of NGC 1068.

4.2.3. Molecular Line Ratios

In order to constrain the excitation conditions and chemistry of the molecular gas, we derive the line ratios for the different molecules and transitions in several ways by accounting for the different angular resolutions (especially with respect to the ^{12}CO($J = 1$–0), ^{13}CO($J = 1$–0), and ^{13}CO($J = 3$–2) emission). Before determining any line ratio, the line emission was brought to the same (lower) angular resolution by using a UV taper; this seems appropriate for most of the lines as we recovered most of the emission with the interferometric observations. Also, we compute line ratios only for emission coming from the same spatial regions (see Figures 12–14). Figure 12 shows the velocity-integrated line ratios between various combinations of the molecular lines. Separating the eastern and western knots spatially, we derive spatially averaged line ratios from Figure 12, which are listed in Table 6. Note that the values in Table 6 might vary from those derived from Tables 4 and 5. However, the differences can easily be explained by different averaging sequences (i.e., first in space, then in velocity versus first in velocity, then in space) for Table 5, the usage of an elliptical Gaussian fit[15] for Table 4 as opposed to spatially averaging without a fit (as done for Table 6) and the different spatial resolutions of the line emission in Tables 4 and 5.

We identify some spatial variance of the different line ratios (mostly by a factor of ∼2–3), which seems to be most pronounced in the ^{12}CO and ^{13}CO line ratios (Figures 12(a), (d), and (o)). The HCN and HCO$^+$ line ratios seem to be more constant over the CND than the ^{12}CO and ^{13}CO line ratios. The higher values are found closer to the position of the AGN for most maps.

In order to investigate whether there might be a velocity (and spatial) dependence on the line ratios, we determined the line-ratio channel maps for the two strongest ^{12}CO transitions ($J =$ 2–1 and J = 3–2) as a function of velocity in Figure 13. We find somewhat higher (i.e., by a factor of $\gtrsim$2) ^{12}CO($J = 3$–2)-to-^{12}CO($J = 2$–1) ratios close to the AGN at velocities around the systemic velocity but also on the eastern knot at high negative velocities ($\lesssim$−130 km s^{-1}). Both knots seem to show (more

[15] Although this is a reasonable first-order fit, the line emission is certainly not exactly of an elliptical Gaussian shape, so some of the emission is not well reproduced by fitting an elliptical Gaussian to the velocity-integrated maps.

Table 6
Molecular Line Ratios for NGC 1068[a] (X[K]/Y[K])

		^{12}CO			^{13}CO			C^{18}O	HCN			HCO$^+$		
X	Y	$J = 1–0$	$J = 2–1$	$J = 3–2$	$J = 1–0$	$J = 2–1$	$J = 3–2$	$J = 2–1$	$J = 1–0$	$J = 2–1$	$J = 3–2$	$J = 1–0$	$J = 3–2$	$J = 4–3$
						E-knot								
^{12}CO	$J = 1–0$	…	0.3 ± 0.2	0.2 ± 0.1	20 ± 10	…	…	…	…	…	…	…	…	…
	$J = 2–1$	2.9 ± 0.3	…	0.3 ± 0.2	…	5.0 ± 3.0	…	17 ± 4	…	…	4.0 ± 2.0	…	7.0 ± 3.0	…
	$J = 3–2$	6.0 ± 3.0	4.0 ± 2.0	…	…	…	25 ± 6	…	…	…	5.0 ± 3.0	…	8.0 ± 3.0	…
^{13}CO	$J = 1–0$	0.05 ± 0.03	…	…	…	0.2 ± 0.1	0.08 ± 0.04	…	…	…	…	…	…	…
	$J = 2–1$	…	0.2 ± 0.1	…	5.0 ± 3.0	…	0.7 ± 0.3	1.4 ± 0.3	…	…	0.3 ± 0.2	…	0.5 ± 0.2	…
	$J = 3–2$	…	…	0.04 ± 0.01	13 ± 4	1.4 ± 0.4	…	…	…	…	0.2 ± 0.1	…	0.5 ± 0.3	…
C^{18}O	$J = 2–1$	…	0.06 ± 0.03	…	…	0.8 ± 0.3	…	…	…	…	…	…	…	…
HCN	$J = 1–0$	…	…	…	…	…	…	…	…	…	…	…	…	…
	$J = 3–2$	…	0.3 ± 0.1	0.14 ± 0.03	…	4 ± 1	4.0 ± 1.0	…	…	…	…	…	…	…
HCO$^+$	$J = 1–0$	…	…	…	…	…	…	…	…	…	…	…	…	…
	$J = 3–2$	…	0.13 ± 0.02	0.07 ± 0.01	…	2.0 ± 0.4	2.0 ± 0.5	…	…	…	0.6 ± 0.3	…	…	1.8 ± 0.9
	$J = 4–3$	…	…	…	…	…	…	…	…	…	…	…	0.6 ± 0.3	…
						W-knot								
^{12}CO	$J = 1–0$	…	0.8 ± 0.7	0.3 ± 0.2	50 ± 30	…	…	…	…	…	…	…	…	…
	$J = 2–1$	1.5 ± 0.5	…	0.3 ± 0.2	…	10 ± 2	…	…	…	…	3.4 ± 0.6	…	6.0 ± 1.0	…
	$J = 3–2$	4.0 ± 2.0	3.0 ± 2.0	…	…	…	25 ± 6	…	…	…	6.0 ± 1.0	…	11 ± 2	…
^{13}CO	$J = 1–0$	0.02 ± 0.01	…	…	…	0.13 ± 0.06	…	…	…	…	…	…	…	…
	$J = 2–1$	…	0.10 ± 0.02	…	8.0 ± 4.0	…	…	…	…	…	0.4 ± 0.2	…	0.6 ± 0.3	…
	$J = 3–2$	…	…	0.04 ± 0.01	…	…	…	…	…	…	…	…	…	…
C^{18}O	$J = 2–1$	…	…	…	…	…	…	…	…	…	…	…	…	…
HCN	$J = 1–0$	…	…	…	…	…	…	…	…	…	…	…	…	…
	$J = 3–2$	…	0.3 ± 0.1	0.2 ± 0.1	…	3.0 ± 2	…	…	…	…	…	…	1.9 ± 0.5	…
HCO$^+$	$J = 1–0$	…	…	…	…	…	…	…	…	…	…	…	…	…
	$J = 3–2$	…	0.17 ± 0.03	0.09 ± 0.02	…	1.7 ± 0.4	…	…	…	…	0.5 ± 0.3	…	…	…
	$J = 4–3$	…	…	…	…	…	…	…	…	…	…	…	…	…
						Total								
^{12}CO	$J = 1–0$	…	0.3 ± 0.2	0.3 ± 0.2	40 ± 20	…	…	…	…	…	…	…	…	…
	$J = 2–1$	2.0 ± 1.0	…	0.3 ± 0.2	…	8 ± 3	…	94 ± 6	…	…	4.0 ± 2.0	…	9.0 ± 4.0	…
	$J = 3–2$	4.0 ± 2	4.0 ± 2.0	…	…	…	41 ± 2.0	…	…	…	8.0 ± 4.0	…	16 ± 1	…
^{13}CO	$J = 1–0$	0.04 ± 0.02	…	…	…	0.17 ± 0.04	0.2 ± 0.1	…	…	…	…	…	…	…
	$J = 2–1$	…	0.2 ± 0.1	…	6.0 ± 1.0	…	1.0 ± 0.5	…	…	…	0.3 ± 0.2	…	0.6 ± 0.3	…
	$J = 3–2$	…	…	0.025 ± 0.001	4.0 ± 1.0	0.7 ± 0.3	…	…	…	…	0.2 ± 0.1	…	0.4 ± 0.2	…
C^{18}O	$J = 2–1$	…	0.011 ± 0.001	…	…	0.2 ± 0.1	…	…	…	…	…	…	…	…
HCN	$J = 1–0$	…	…	…	…	…	…	…	…	…	…	…	…	…
	$J = 2–1$	…	…	…	…	…	…	…	…	…	…	…	…	…
	$J = 3–2$	…	0.3 ± 0.1	0.12 ± 0.01	…	3.0 ± 0.3	5.0 ± 3.0	…	…	…	…	…	1.9 ± 0.2	…
HCO$^+$	$J = 1–0$	…	…	…	…	…	…	…	…	…	…	…	…	…
	$J = 3–2$	…	0.11 ± 0.01	0.08 ± 0.02	…	1.8 ± 0.1	3.0 ± 0.2	…	…	…	0.5 ± 0.3	…	…	1.6 ± 0.8
	$J = 4–3$	…	…	…	…	…	1.6 ± 0.1	…	…	…	…	…	0.6 ± 0.3	…

Note.
[a] The line ratios were derived by spatially averaging over the respective regions from the velocity-integrated line ratio maps from Figure 12. The errors therefore denote the standard deviation from the averaged values. Please note that in some cases, the line ratios might vary from those estimated in Tables 4 and 5. See the text for discussion.

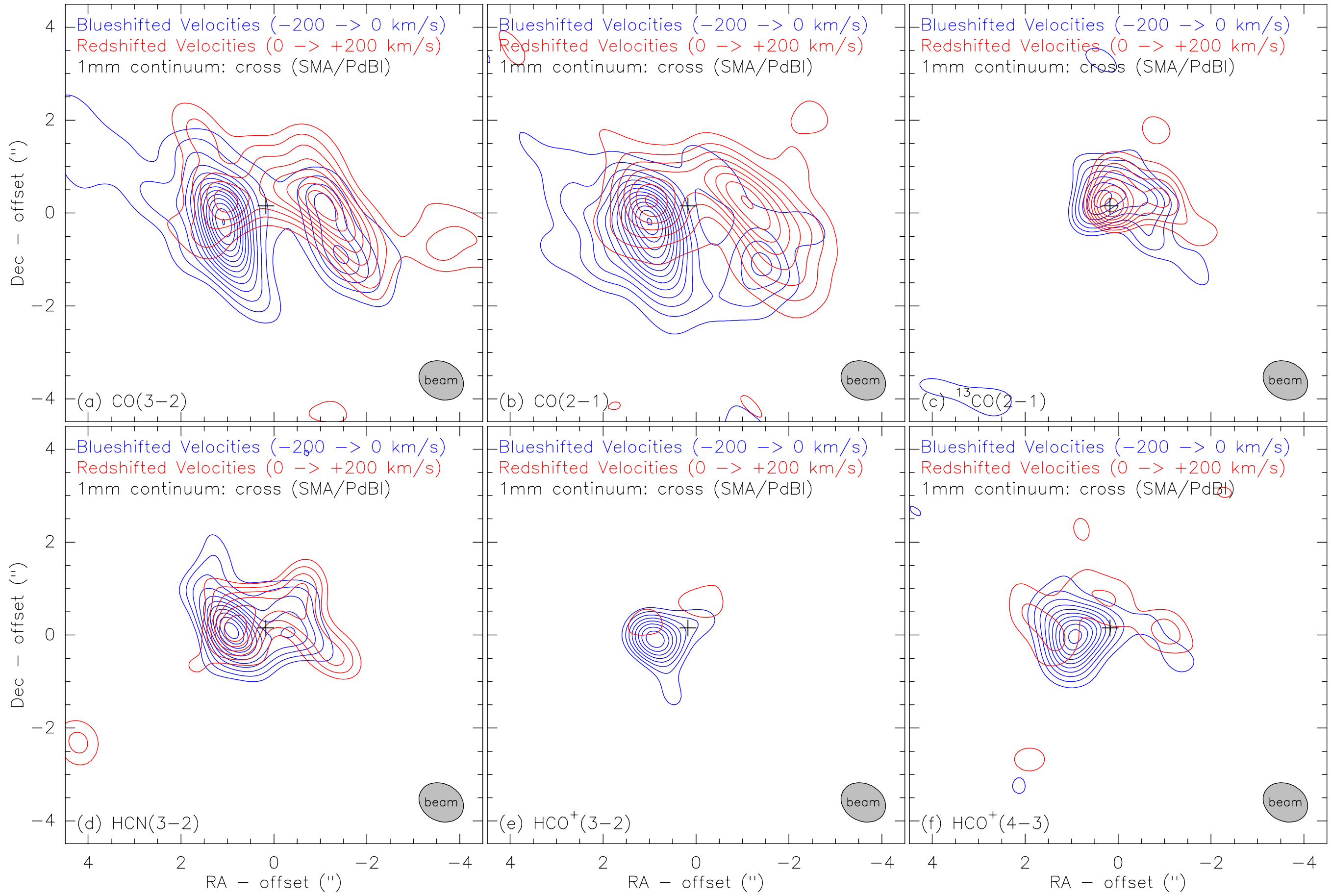

Figure 6. Redshifted and blueshifted emission of NGC1068. Contours are in steps of: (a) from 7σ by 5σ with $1\sigma = 2.0$ Jy km s^{-1}; (b) from 5σ by 5σ with $1\sigma = 0.9$ Jy km s^{-1}; (c) from 4σ by 1σ with $1\sigma = 0.5$ Jy km s^{-1}; (d) from 3σ by 1σ with $1\sigma = 1.9$ Jy km s^{-1}; (e) from 3σ by 1σ with $1\sigma = 2.3$ Jy km s^{-1}; and (f) from 2σ by 1σ with $1\sigma = 1.4$ Jy km s^{-1}.

(A color version of this figure is available in the online journal.)

or less) the same velocity and spatial behavior as can be seen in Figure 14. This plot shows the spatially averaged ^{12}CO($J =$ 3–2)-to-^{12}CO($J =$ 2–1) line ratios for the eastern and western knots as a function of velocity. The two curves follow each other nicely except for velocities between −120 and −140 km s^{-1} for which the eastern knot exposes higher values (by a factor of two). The error bars denote the variance of each averaged value, which in most cases indicates variation by a factor of 1.5.

5. DISCUSSION

5.1. Spectral Energy Distribution of the Continuum Emission

The nature of the continuum emission (from IR over submillimeter to centimeter wavelengths) represents a highly debated and complicated matter for NGC 1068, and recently has been experiencing a revival because of newly published Very Large Telescope Interferometer/MIDI (i.e., IR) and radio data (e.g., Hönig et al. 2008; Cotton et al. 2008). As mentioned in the previous section, the radio continuum emission splits into several components—a jet plus a counterjet and a core component (S1) associated with the AGN itself. While the emission from the jet is certainly pure non-thermal synchrotron emission, as supported by its steep continuum spectrum (e.g., Gallimore et al. 2004; Cotton et al. 2008), the nature of the emission from S1 is highly controversial. Gallimore et al. (2004) already rule out synchrotron emission as the origin of the continuum spectrum of S1 and discuss electron-scattered synchrotron emission as well as thermal free–free absorption as alternatives. While Krips et al. (2006) present arguments for electron-scattered synchrotron emission based on a turnover observed between centimeter and millimeter data, Cotton et al. (2008) instead support the thermal free–free absorption model. A highly complicating factor in this discussion is certainly the mismatch in angular resolution between the centimeter, millimeter, and IR data. As discussed in Krips et al. (2006) and this paper, the millimeter continuum emission is contaminated by emission from the jet at angular resolutions of $\gtrsim 1''$, introducing large uncertainties into the estimate of S1's flux (compare Hönig et al. 2008; Cotton et al. 2008; Krips et al. 2006) due to the lack of angular resolution. However, the previous estimate of the 1.3 mm continuum flux of (10 ± 4) mJy in Krips et al. (2006), translating into (9 ± 4) mJy at 1.0 mm, is very similar to the measured 1.0 mm continuum flux of (13 ± 2) mJy from our high angular resolution SMA observations. Given the unresolved nature of the latter, jet emission no longer seems to be significant at this angular resolution (see also Figure 1 in Cotton et al. 2008), although the obtained angular resolution is still an order of magnitude larger than that at centimeter wavelengths.

Also taking the new 850 μm (UN) continuum flux measurements into account, we recomputed the spectral energy distribution (SED) and replotted the models used by Hönig et al. (2008) and Krips et al. (2006). We therefore base our graphs on

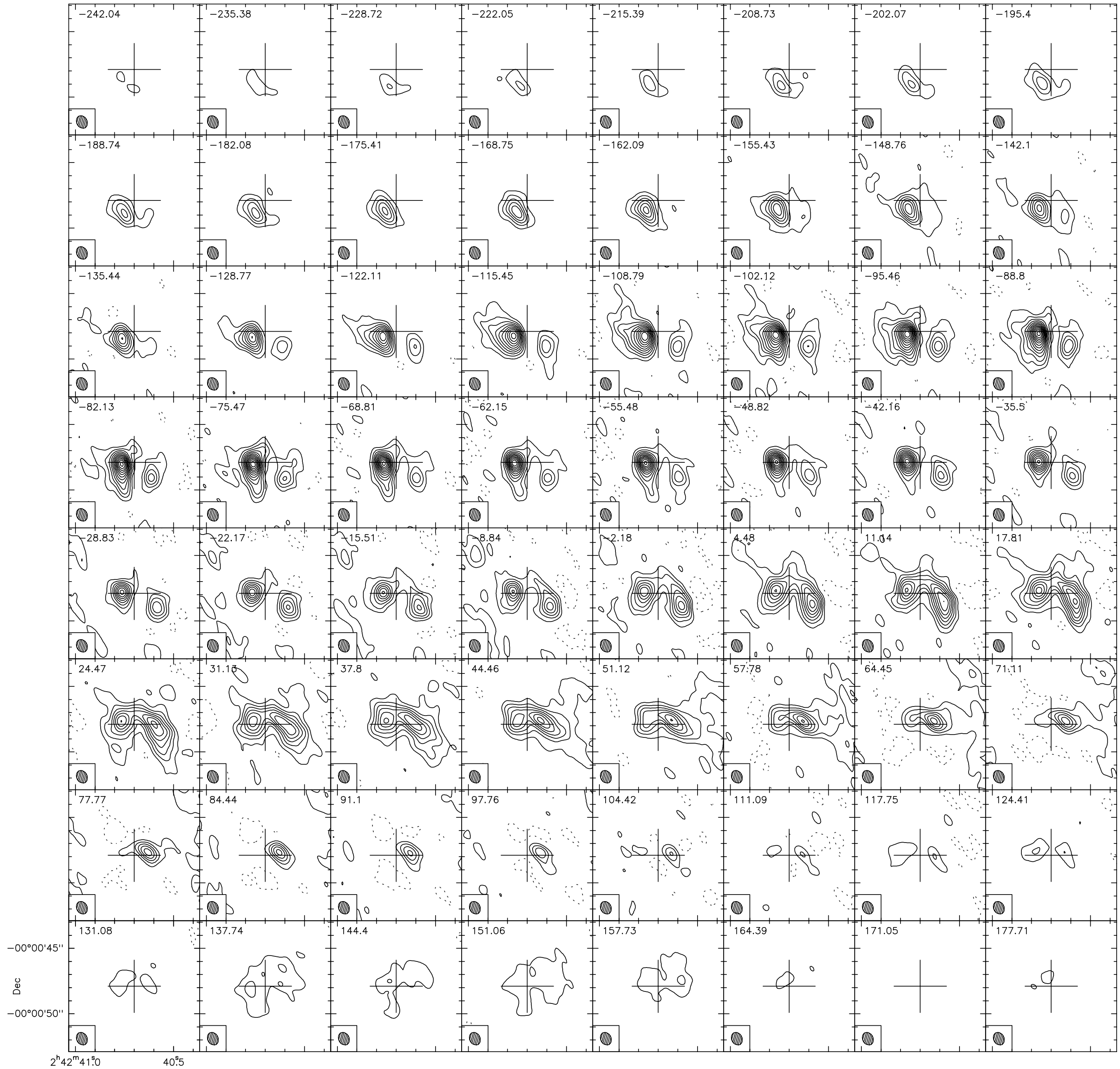

Figure 7. Channel maps of the $^{12}CO(J = 2–1)$ emission in NGC 1068. Please note that the $^{12}CO(J = 2–1)$ data were resampled to match the spectral resolution of the $^{12}CO(J = 3–2)$ data and facilitate a comparison, especially with respect to the line-ratio channel map in Figure 13. Contour spacing is in steps of $5\sigma = 37.4$ mJy beam^{-1}. We use a spectral resolution of ∼7 km s^{-1}. The zero channel corresponds to $\upsilon_{\rm LSR} = 1137$ km s^{-1} of NGC 1068.

the formula and parameters specified in Equations (2)–(5) and Tables 2 and 3 in Hönig et al. (2008) and Equations (1) and (2) and Figure 3 in Krips et al. (2006). The results are shown in Figures 15(a)–(c). We marked all data points with a circle for which the obtained angular resolution of the observations did not exceed 1″.[16] We also fitted a two-temperature gray body to the IR data in order to estimate the contribution of thermal dust emission to the submillimeter-continuum emission. Although this gray-body fit is certainly not as sophisticated as the clumpy torus model used in Hönig et al. (2008), it represents a reasonable approximation as demonstrated by the good match to the IR data points.

As can be seen in Figures 15(b) and (c), the models used by Hönig et al. (2008) significantly overestimate the observed 1 mm (UN) flux by a factor of two to three, although they correctly reproduce the 850 μm one. It seems that both the electron-scattered synchrotron emission model in Figure 15(a) and the thermal free–free emission model in Figure 15(c) need the extra contribution from the thermal dust emission to correctly reproduce the 850 μm (UN) flux, while the synchrotron model in Figure 15(b) does not require it. Thus, it appears to be very likely indeed that the continuum emission is dominated by thermal dust emission starting at wavelengths $\lesssim$850 μm, as posited above.

[16] Note that this is true for all data points except the one at 3 mm. The encircled S1 data point has been estimated at 3 mm, not observed. We added this data point for consistency reasons only.

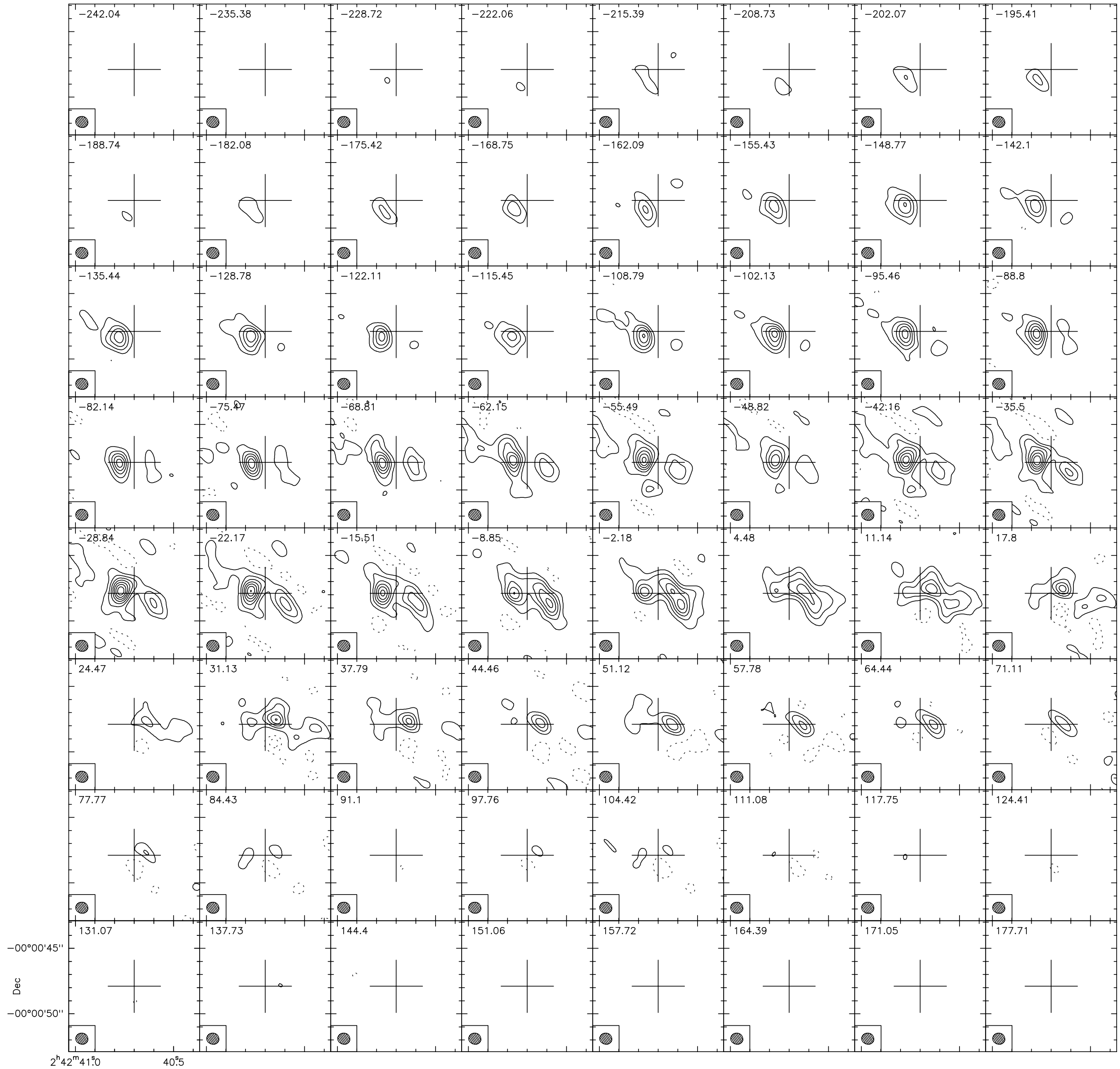

Figure 8. Channel maps of the $^{12}CO(J = 3–2)$ emission in NGC 1068. We use a spectral resolution of $\sim$7 km s^{-1} and the original spatial resolution from the observations. Contour spacing is in steps of $5\sigma = 400$ mJy beam^{-1}. The zero channel corresponds to $\upsilon_{\rm LSR} = 1137$ km s^{-1} of NGC 1068.

Based on the 1 mm (UN) flux, it seems that the model best reproducing the SED at centimeter and millimeter wavelengths is the electron-scattered synchrotron emission; the thermal free–free absorption seems to overpredict the 1 mm flux. However, observations of the continuum emission in NGC 1068 have to be conducted at similarly high angular resolutions ($\ll$0$''\!$.5), in order to dispel all remaining doubts, although the new millimeter observations presented in this paper are already a step in the right direction.

5.2. Dynamics of the Molecular Gas

In previous studies, the complex kinematic behavior of the molecular gas has been thought to be a consequence of a warped disk. A warped disk has been modeled by a tilted ring (e.g., Schinnerer et al. 2000). However, the spatial overlap between the redshifted and blueshifted emission (i.e., the existence of highly non-circular motions) cannot be reproduced by these tilted ring models because they are based on circular motions and thus cannot account for non-circular motions of the gas (within the plane).

Even though we cannot rule out a warped disk scenario in which part of the gas could be trapped in elliptical orbits producing the non-circular motions, we want to propose an alternative approach following recent findings on the H_2(1–0) S(1) emission at scales of 100–150 pc by Müller-Sànchez et al. (2009) and the model proposed by Galliano & Alloin (2002). The nature of the dynamics displayed in Figures 4–8 could also be explained by the following scenario: a rotating disk plus an outflow of the disk gas due to shocks and/or a CND–jet

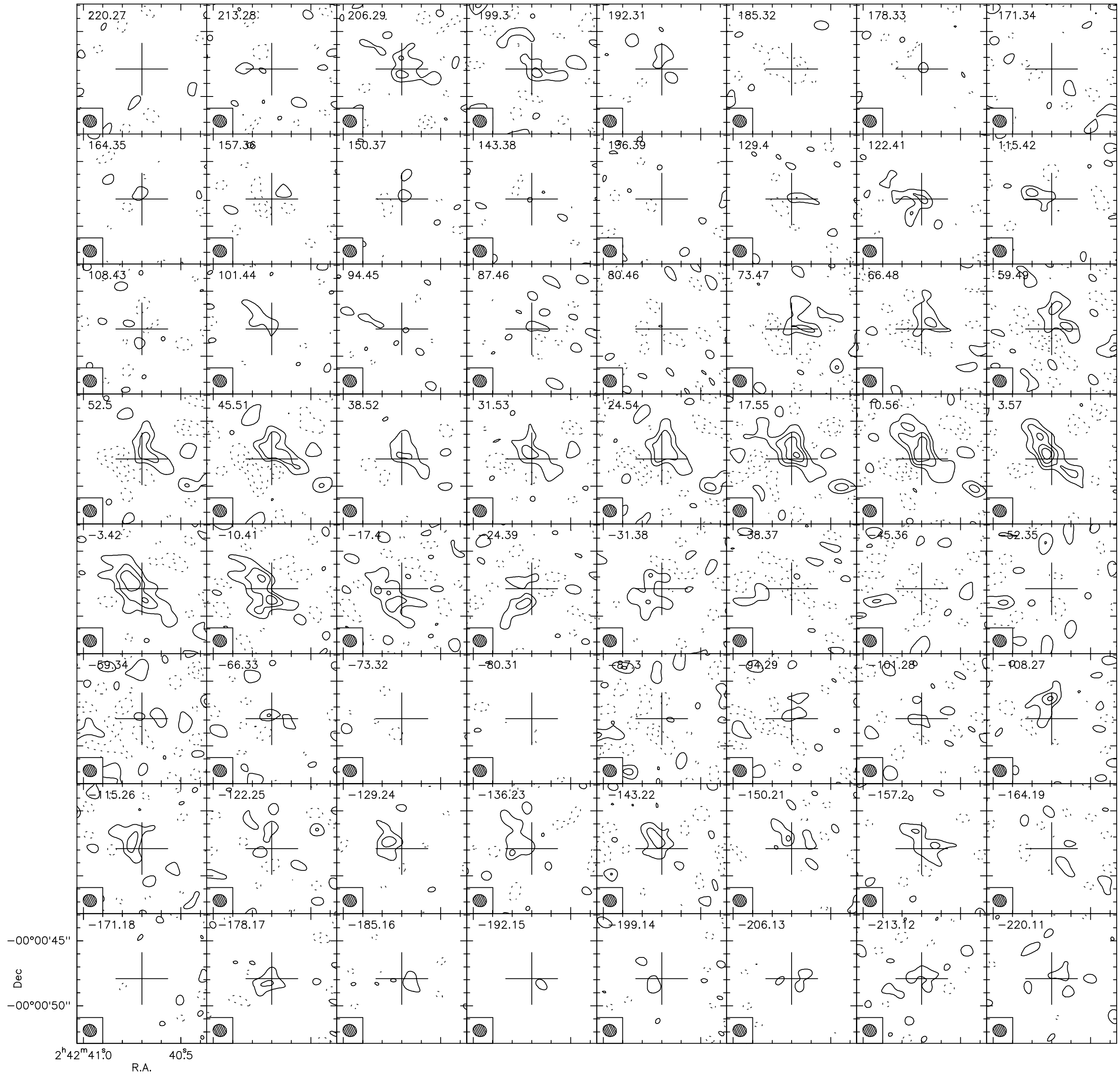

Figure 9. Channel maps of the ^{13}CO($J = 2$–1) emission in NGC 1068. We use spectral resolution of $\sim$7 km s^{-1}. Contour spacing is in steps of $2\sigma = 11$ mJy beam^{-1}. The zero channel corresponds to $v_{\rm LSR} = 1137$ km s^{-1} of NGC 1068.

interaction. This hypothesis seems to gain further support when considering not only the H_2 1–0 $S(1)$ map (Müller-Sànchez et al. 2009, see their Figure 4), but also the 12 μm map (Bock et al. 2000, see their Figure 4), and the 5 cm radio continuum map (Gallimore et al. 2004, see their Figure 1). The H_2 1–0 $S(1)$ and 12 μm emission follows nicely that of the radio jet in the inner 1″ (north/northeast direction), which seems to interact with emission from the molecular gas in the CND at $\pm$1″–2″ in the northern part (see the next subsection); both the blueshifted and redshifted components associate with the non-circular motions to the east and west of where the jet goes through or lies in front of the CND (see also the case of M51; Matsushita et al. 2007, 2004). As the jet shows a biconical structure with a change in direction close to the CND, it is reasonable to believe that part of it indeed hits the CND (see also Kraemer et al. 1998). Such an interaction could easily produce a shock through/along the CND (at least in the northern part, i.e., the bridge between the eastern and western knots) feeding the assumption that some part of the molecular gas in the ring/disk might be blown outward.

Other causes of expanding/shocked gas include hypernovae explosions, stellar winds from a super stellar cluster as suspected in some nearby SB galaxies (such as NGC 253 or M82; Sakamoto et al. 2006; Matsushita et al. 2000), or cloud–cloud collisions within the CND (i.e., within the inner Lindblad resonance; see García-Burillo et al. 2010). However, they seem rather unlikely since the CND of NGC 1068 does not show any signs of SB activity and the expansion seems to be too "ordered," (i.e., too symmetric) to be caused by highly chaotic cloud–cloud collisions. Also, we cannot entirely rule out that the dynamics we see in the molecular gas are due to inflowing rather

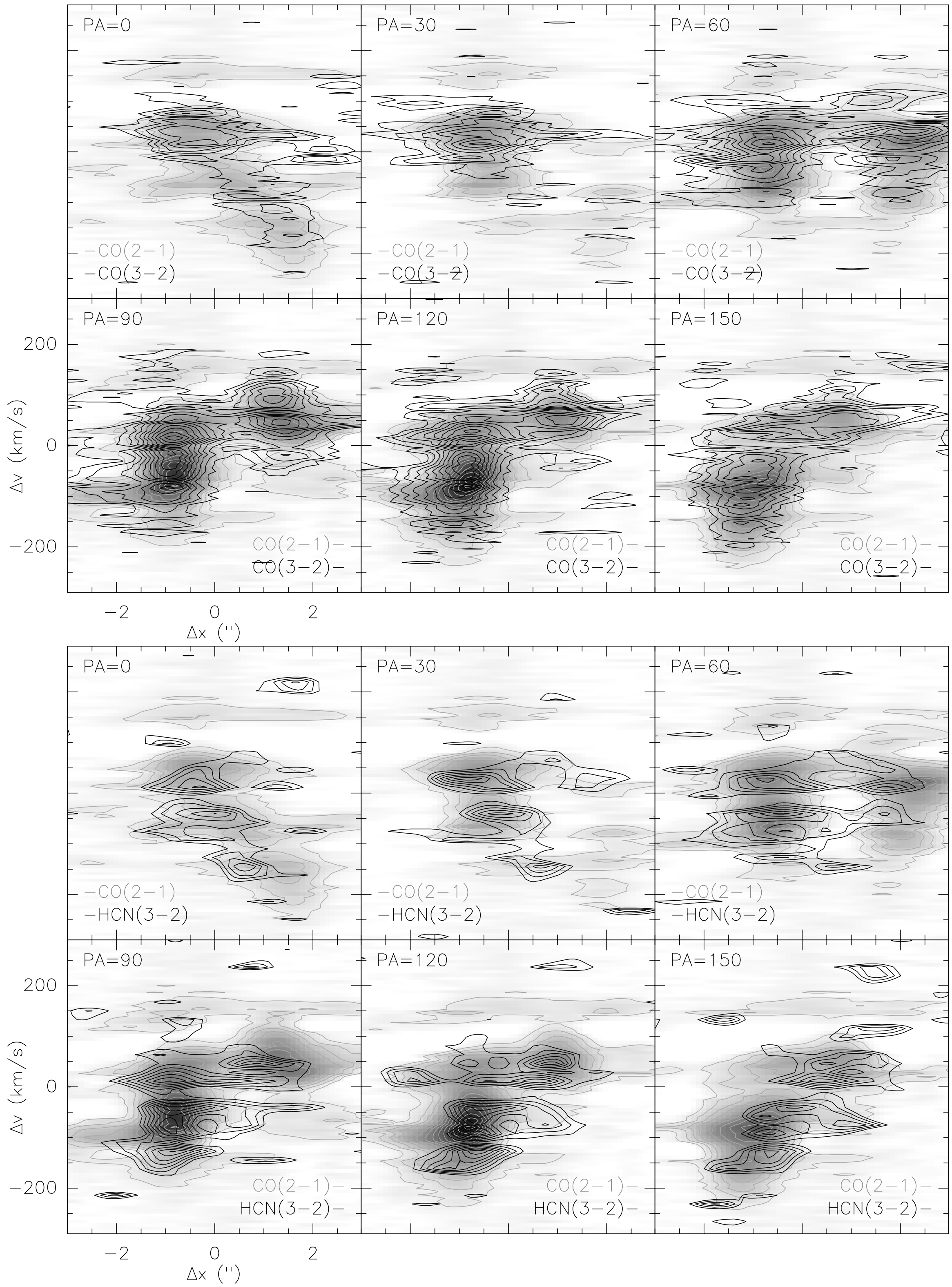

Figure 10. Position–velocity diagram of NGC 1068 for the ^{12}CO(J = 2–1) (gray scale), ^{12}CO(J = 3–2) (black contours, top), and HCN(J = 3–2) (black contours; bottom) emission.

than outflowing gas, especially since indications of inflowing gas along the jet within the central ∼70 pc (i.e., on scales smaller than the CND) have already been presented in previous studies (see Müller-Sànchez et al. 2009). However, based on the appearance of the molecular gas within the disk (the ring-like structure with an apparent void of gas in the inner part), we favor the jet–gas interaction (on a scale of 100–150 pc) rather than an inflow scenario. An outflow on a scale of 100–150 pc is not necessarily contradictory to an inflow scenario on the scale of $\lesssim$70 pc proposed by Müller-Sànchez et al. (2009). The jet–gas interaction could equally drag gas outward on scales larger than 100 pc but trigger an inflow at smaller scales, depending

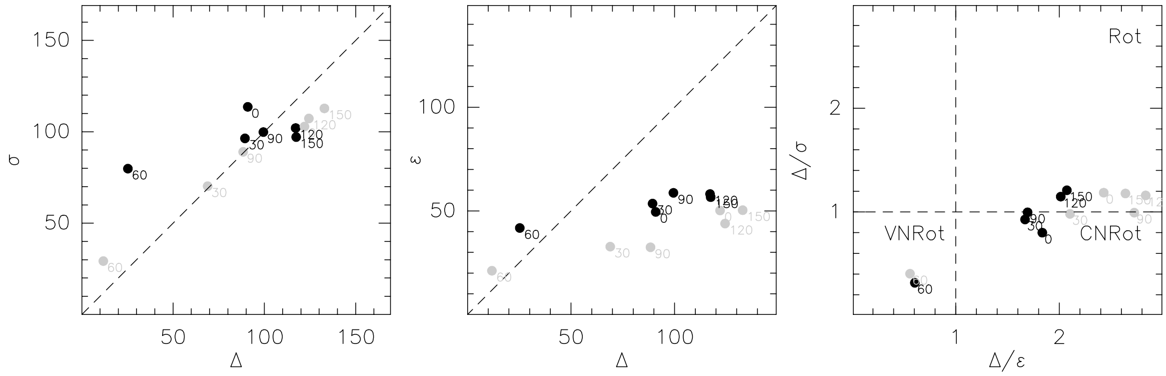

Figure 11. Parameterization of the kinematics in the CND of NGC 1068 for the ^{12}CO($J = 2$–1) emission (black filled data points) taken along the slits at different P.A.s (at 0°, 30°, 60°, 90°, 120°, and 150°). σ is the average line-of-sight velocity dispersion, ϵ is the rms variation of the velocity from point to point, and Δ is the rotational velocity along each slit (see Section 5.2 for a more detailed description). VNRot = violent non-rotators, CNRot = calm non-rotators, and Rot = rotators. The filled gray data points were determined from the model discussed in Section 5.2.

on the type of interaction between the jet and the molecular clouds. However, higher angular resolution observations at subarcsecond angular resolution (as are possible with ALMA) will certainly help to distinguish between the different scenarios.

Based on this alternative approach, we tried to reproduce the molecular gas dynamics with a very simplistic model that included a dominant (Keplerian) rotating disk plus an outflow of some of the disk gas. We therefore assumed a velocity gradient of $\Delta v_0 = 200$ km s^{-1}, a radius of $\sim 1\farcs2$, and an inclination of $\sim 60°$ for the rotating disk. We additionally added to the model a slight ellipticity of 5% and an asymmetry ratio between the eastern and western parts of 1:0.7. The outflow was approximated by a slightly expanding elliptical ring. We assumed the same ellipticity of 5% as before and that the expansion starts at the inner radius of the disk. The expansion rate (H) was chosen to be 200 km s^{-1} per 1″ or, equivalently, 67 pc (i.e., $H = 3$ km s^{-1} pc^{-1}); this value is similar to what has been estimated for M51 (2.2 km s^{-1} pc^{-1}; Matsushita et al. 2007). We also introduced a slight asymmetry ratio of 1:0.9 between the blueshifted and redshifted emission. We further assumed that up to $\sim$30% of the disk gas is expanding. Most of these values chosen for the model parameters were almost instantly obvious from the observations, especially the velocities and radii. We hence used them as starting values and then scanned through a reasonable parameter space for the optimal combination of input values that best matched the observed maps. However, given the larger number of parameters used in this model and hence the many degrees of freedom, we did not actually conduct a true fit to the data but rather a fit "by eye." The results of this "best-fit" model are displayed and compared to the ^{12}CO($J = 2$–1) emission in Figures 16–20. Indeed, the major dynamical characteristics of the molecular gas emission can be reproduced by this simplistic model, supporting the hypothesis of an additional gas outflow. Also, using the same kinematic parameterization for the model as used for the ^{12}CO emission (see Figure 11), we find very similar ratios between the observed and simulated emission. We have to stress that this suggestion does not exclude a warped CND, but it is not needed for this model.

It is interesting to note as further support for our approach that the distribution of the HCN($J = 3$–2) emission almost exactly matches that of the H_2 1–0 $S(1)$ emission in the CND, even better than the ^{12}CO($J = 2$–1) emission (see Figure 1 in Müller-Sànchez et al. 2009). Similar to the H_2 map, which indicates that the brightest emission is toward the north, most of the HCN emission is also found toward the northern part of the CND where most of the potentially shocked gas would lie. Thus, one would expect the densest (and hottest) part of the gas to be in that area (see the next section).

5.3. Excitation Conditions of the Gas

The line ratios derived from the interferometric maps, especially for the HCN, HCO$^+$, and ^{12}CO emission (Figure 12 and Table 6), are consistent with previous findings from single-dish observations (e.g., Krips et al. 2008). They support a picture in which the molecular gas in the CND is relatively dense ($n(H_2) \leqslant 10^{4.5}$) and warm ($T_k > 40$ K) with potentially higher than normal (i.e., in Galactic giant molecular clouds) HCN abundances (Z(HCN) = [HCN]/[H_2]) of Z(HCN) = 1–50 × $Z_{galactic}$(HCN) ($Z_{galactic}$(HCN) = 2 × 10^{-8}; e.g., Irvine et al. 1987). Krips et al. (2008) argue that the high HCN-to-^{12}CO($J =$ 1–0) and HCN-to-^{13}CO($J = 1$–0) ratios in NGC 1068 can be explained by higher than normal HCN abundances due to an XDR (see also Usero et al. 2004; Sternberg et al. 1994) and/or higher gas temperatures leading to hypo-excited CO($J = 1$–0) emission. The latter explanation is supported by decreasing HCN-to-CO line ratios with an increasing rotational number J. However, strong constraints on the kinetic temperatures could not be set based on the single-dish observations alone. Also, most single-dish observations are unable to unambiguously distinguish between the molecular gas emission in the center and that in the star-forming spiral arms, complicating any interpretation of the data. Furthermore, most of the interferometric data previously published focuses on ^{12}CO at moderate angular resolution and only two of its transitions.

The new interferometric maps, obtained for several transitions and molecules at sufficiently high angular resolution, overcome some of the shortcomings of previous observations/analyses.

Below, we discuss results from simulations of the excitation conditions of the molecular gas carried out with the radiative transfer code RADEX developed by Van der Tak et al. (2007). Please note that we did not find a significant difference when using the Large-Velocity-Gradient (LVG) code in MIRIAD or the RADEX code. Given simplified simulations with RADEX, we decided to use that in this paper as opposed to Krips et al. (2008) in which the LVG was used.

RADEX offers three different possibilities for the escape probability method: (1) a uniform sphere, (2) an expanding sphere (LVG), and (3) a plane parallel slab (shock). We used all three methods but did not find significant differences for our data between them. Thus, in order to keep the interpretation

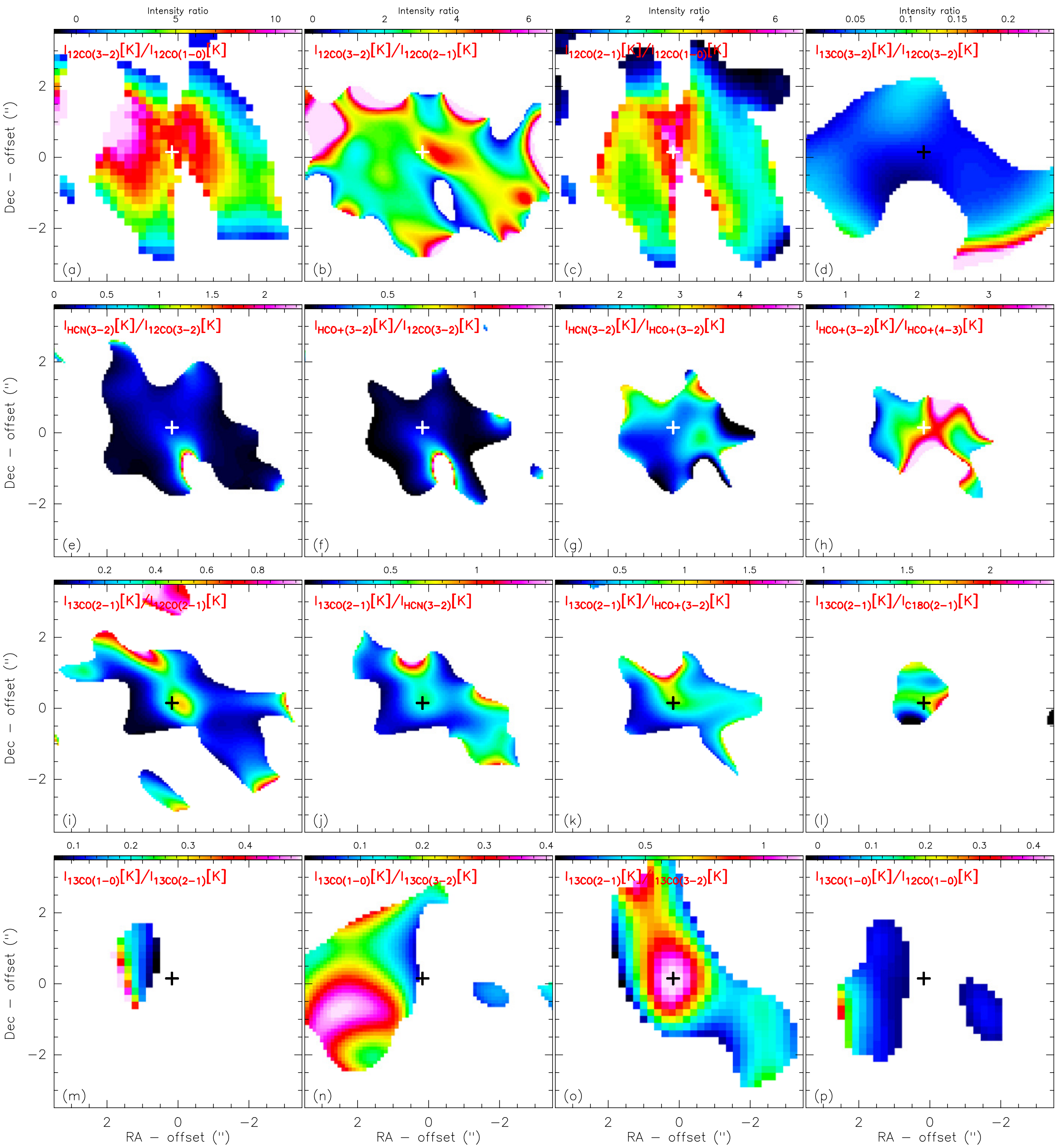

Figure 12. Velocity-integrated molecular line intensity ratios for NGC 1068 above a $\geqslant 1\sigma$ threshold. The white cross marks the position of the millimeter continuum emission that is associated with the AGN. The different line ratios are: (a) ^{12}CO($J = 3$–2)-to-^{12}CO($J = 1$–0); (b) ^{12}CO($J = 3$–2)-to-^{12}CO($J = 2$–1); (c) ^{12}CO($J = 2$–1)-to-^{12}CO($J = 1$–0); (d) ^{12}CO($J = 3$–2)-to-^{13}CO($J = 3$–2); (e) HCN($J = 3$–2)-to-^{12}CO($J = 3$–2); (f) HCO$^+$($J = 3$–2)-to-^{12}CO($J = 3$–2); (g) HCN($J = 3$–2)-to-HCO$^+$($J = 3$–2); (h) HCO$^+$($J = 3$–2)-to-HCO$^+$($J = 4$–3); (i) ^{13}CO($J = 2$–1)-to-^{12}CO($J = 2$–1); (j) ^{13}CO($J = 2$–1)-to-HCN($J = 3$–2); (k) ^{13}CO($J = 2$–1)-to-HCO$^+$($J = 3$–2); (l) ^{13}CO($J = 2$–1)-to-C^{18}O($J = 2$–1); (m) ^{13}CO($J = 1$–0)-to-^{13}CO($J = 2$–1); (n) ^{13}CO($J = 1$–0)-to-^{13}CO($J = 1$–0); (o) ^{13}CO($J = 2$–1)-to-^{13}CO($J = 3$–2) and (p) ^{13}CO($J = 1$–0)-to-^{12}CO($J = 1$–0).

as simple as possible, we discuss the results with respect to a uniform sphere below.

We carried out simulations with RADEX for each molecule using the following grid of parameters (dimension: $51 \times 51 \times 51$).

1. Kinetic temperature: $T_{\rm kin} = 1$–500 K.
2. Gas density: $n(\rm H_2) = 10^3$–10^7 cm^{-3}.
3. Column density: $N(^{12}\rm CO) = 10^{13}$–10^{21} cm^{-2}.

We define the abundance ratio between one molecule (MOL1) and another (MOL2) as $X^{\rm MOL1}_{\rm MOL2} \equiv Z(\rm MOL1)/Z(\rm MOL2)$ with $Z(\rm MOL1) \equiv [\rm MOL1]/[\rm H_2]$. For the different molecular abundance ratios we assume the following ranges.

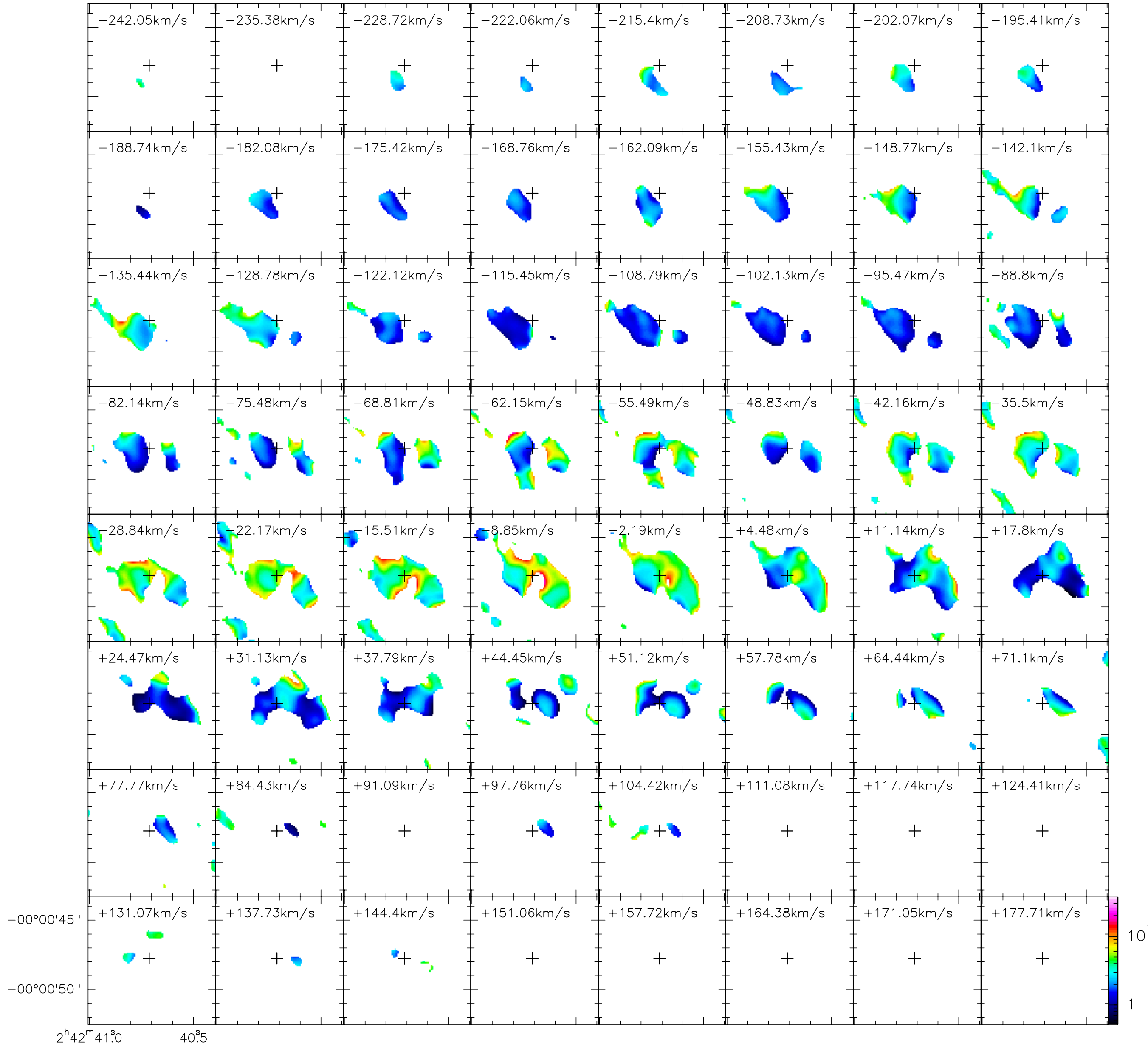

Figure 13. ^{12}CO(J = 3–2)-to-^{12}CO(J = 2–1) line ratio above a 4σ threshold for each line.

1. Abundance ratios:

$$X^{^{12}CO}_{^{13}CO} \simeq 6\text{–}1000, \text{ and}$$
$$X^{HCN}_{HCO^+} \simeq 1\text{–}500.$$

The ranges were chosen because they span the abundance ratios found in different (Galactic and extragalactic) environments. In the Milky Way, typical values of the ^{12}C/^{13}C abundance ratio are ∼20, which increase to values of 80–100 in the outer parts of the Galaxy (e.g., Wilson & Rood 1994; Wilson & Matteucci 1992). Nearby SB galaxies and ultraluminous infrared galaxies (ULIRGs) show somewhat higher ^{12}C/^{13}C abundance ratios (>30) than those found in the Galactic center (e.g., NGC 253, M82, IC 342, NGC 4945, NGC 6240; see Greve et al. 2009; Henkel et al. 1998, 1994, 1993; Henkel & Mauersberger 1993) with Arp 220 being the exception. Greve et al. (2009) find a very low abundance ratio of only eight for this galaxy. Furthermore, some high-redshift galaxies also seem to exhibit rather high ^{12}C/^{13}C values of >30 as determined for the ISM in the gravitational lens of PKS 1830−211 (Muller et al. 2006) or the Cloverleaf quasar (Henkel et al. 2010). Values of $X^{HCN}_{HCO^+}$ show an equally large scatter ranging from unity in star-forming regions in the Milky Way (such as Orion and SgrB2; see Blake et al. 1987) and nearby SB galaxies/ULIRGs (such as M82, NGC 2146, NGC 253, NGC 4945, NGC 6240, and Arp 220; see Naylor et al. 2010; Greve et al. 2009; Krips et al. 2008; Wang et al. 2004) to ⩾10 in nearby Seyfert galaxies (e.g., Krips et al. 2008).

For the simulations, we concentrate on the region of the CND that contains all molecules. This region corresponds to the bridge between the eastern and the western knots, i.e., the northern part of the CND, and has a size of roughly ∼2″–3″ (≃120–180 pc). This roughly corresponds to up to 50% of the molecular gas in the CND. If jet interaction indeed plays a role in NGC 1068, this will be the region most obviously affected.

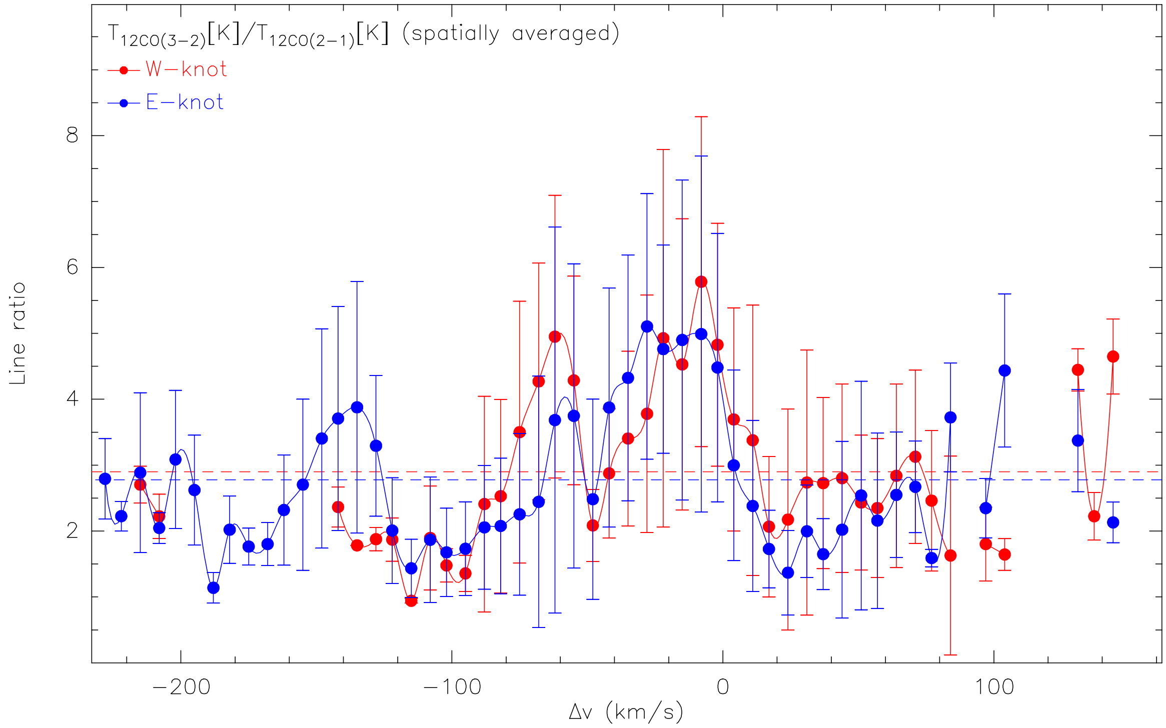

Figure 14. Spatially averaged line ratio for the eastern and western knots as a function of velocity, derived from Figure 13. The error bars denote the variance of each averaged value, which does not exceed 50% in most cases. The missing values for velocities of −120 and −200 km s^{-1} and +100 to +140 km s^{-1} are due to the lack of emission in the respective knot. The dashed lines represent the median of the line ratios for the two knots.

(A color version of this figure is available in the online journal.)

5.3.1. ^{12}CO & ^{13}CO Emission

We conducted a χ^2 test on the RADEX grid by using the observed line ratios for the ^{12}CO and ^{13}CO line emission. Figure 21 shows the parameters for the best χ^2 test for four exemplary abundance ratios (10, 26, 32, and 110) from the aforementioned range; abundance ratios at the lower and higher ends of the range show somewhat higher χ^2 values.

The middle panel shows the lowest χ^2 found in each range of column densities and abundance ratios. The lower and upper panels show the respective lower and upper limits of the column density for which a reasonably low χ^2 still indicated the range in column densities.

The availability of the three lowest transitions for ^{12}CO and ^{13}CO allows us to set tight constraints on $T_{\rm kin}$, $n(H_2)$, and $N(^{12}CO)$. The observed CO line ratios most impressively restrict the kinetic temperatures to well above 200 K. This strengthens previous indications of warm/hot ($T_{\rm kin}$ > 50 K) molecular gas in the CND of NGC 1068 (Kamenetzky et al. 2011; Krips et al. 2008; Matsushita et al. 1998; Sternberg et al. 1994) but is much higher than the temperature found by Tacconi et al. (1994). However, Tacconi et al. (1994) base their simulations on single-dish data that cannot distinguish well between emission from the star-forming ring/spiral arms and the CND. Especially the ^{13}CO(J = 1–0) emission might be overestimated for the CND, which, obviously, is hardly detected in the interferometric map despite the high sensitivity of the observations. The lowest χ^2 is actually found for kinetic temperatures around 450 K, which seems to be fairly high. Although we used a one-gas component model due to the lack of sufficient observational constraints (i.e., higher J CO transitions with $J_{\rm upper} \geqslant 4$), we do not expect all of the gas to be at these high kinetic temperatures but rather a fraction of the gas in the northern part of the bridge. It seems likely that by using a two-temperature model for the molecular gas, we may find slightly lower maximum temperatures. However, this necessitates either the inclusion of CO data at higher J transitions or using so-called molecular thermometers (such as H_2CO or NH_3; see Ao et al. 2011). High kinetic temperatures would be expected in several scenarios, among them shocks as well as heating through X-ray radiation from the AGN (e.g., Meijering et al. 2007; Meijering & Spaans 2005). Nevertheless, a significant fraction (≫10%–20%) of the warm molecular gas in this bridge region seems to exhibit high kinetic temperatures, which is a much larger fraction than found thus far (for the overall molecular gas reservoir) in SB and other Seyfert galaxies (⩽30%; see, for instance, Roussel et al. 2007; Dale et al. 2005; Rigopoulou et al. 2002).

The density is also well constrained and is found to be in the range of $10^{3.5}$–$10^{4.5}$ cm^{-3}, consistent with previous findings (Krips et al. 2008; Matsushita et al. 1998). Considering the range of assumed abundance ratios, the column density of ^{12}CO approximately spans a range between $\sim 10^{17.0}$ cm^{-2} and $10^{19.0}$ cm^{-2}. Even though CO might not be the best tracer of the ^{12}C/^{13}C isotopic ratio (e.g., Martín et al. 2010), we assume it to be a first approximation for this ratio. The carbon ratio of 26 found for the absolute lowest χ^2 is similar to the value of 20 measured in the Galactic center (e.g., Wilson & Rood 1994) and lower than that derived toward nearby SBs (e.g., Henkel et al. 1993, 1994; Henkel & Mauersberger 1993). Such ^{13}C enrichment would point toward a highly nuclear processing of the ISM in the central region of NGC 1068.

5.3.2. HCN & HCO$^+$ Emission

In Krips et al. (2008), we carried out an LVG analysis for NGC 1068 based on the HCN and HCO$^+$ single-dish line ratios with kinetic temperatures not exceeding 200 K. As our new

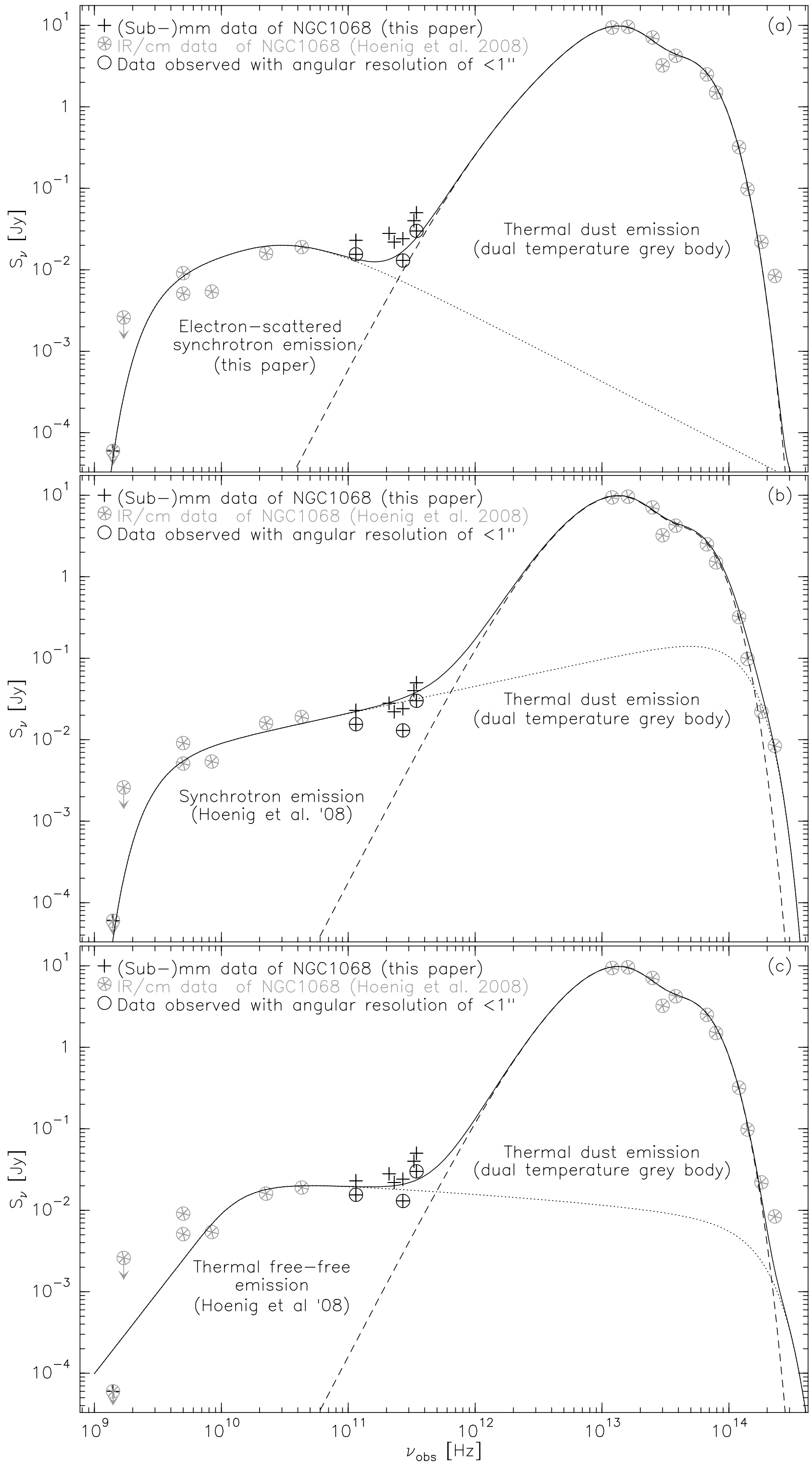

Figure 15. SED of the continuum emission in NGC 1068, based on data from this work, (Krips et al. 2006; black crosses) and (Hönig et al. 2008; gray crosses). The dotted line represents the model for the radio continuum emission (either electron-scattered synchrotron emission (a), synchrotron emission (b), or free–free absorption (c)), the dashed line represents the model for the IR data (a two-temperature gray body, (a)–(c)), and the solid line represents the composite of both, (a)–(c)). The data observed at an angular resolution below 1″ are additionally marked with a circle.

simulations indicate kinetic temperatures lying significantly above 200 K, we repeated the simulations with RADEX, allowing for a larger range in kinetic temperatures. The line fluxes for the HCN and HCO$^+$($J = 1$–0) emission are taken from PdBI observations at ∼1″ angular resolution (García-Burillo et al. 2008), which will be analyzed in more detail in a later paper by A. Usero et al. (2011/2012, in preparation). The results of the RADEX simulations for HCN and HCO$^+$ are shown in Figure 22.

Considering the restrictions for the kinetic temperatures (>200 K), we find solutions (i.e., with low χ^2) with RADEX for which the HCN-to-HCO$^+$ abundance ratio lies in the range $X^{HCN}_{HCO^+} \simeq 10$–500 which is higher than that found in star-forming/

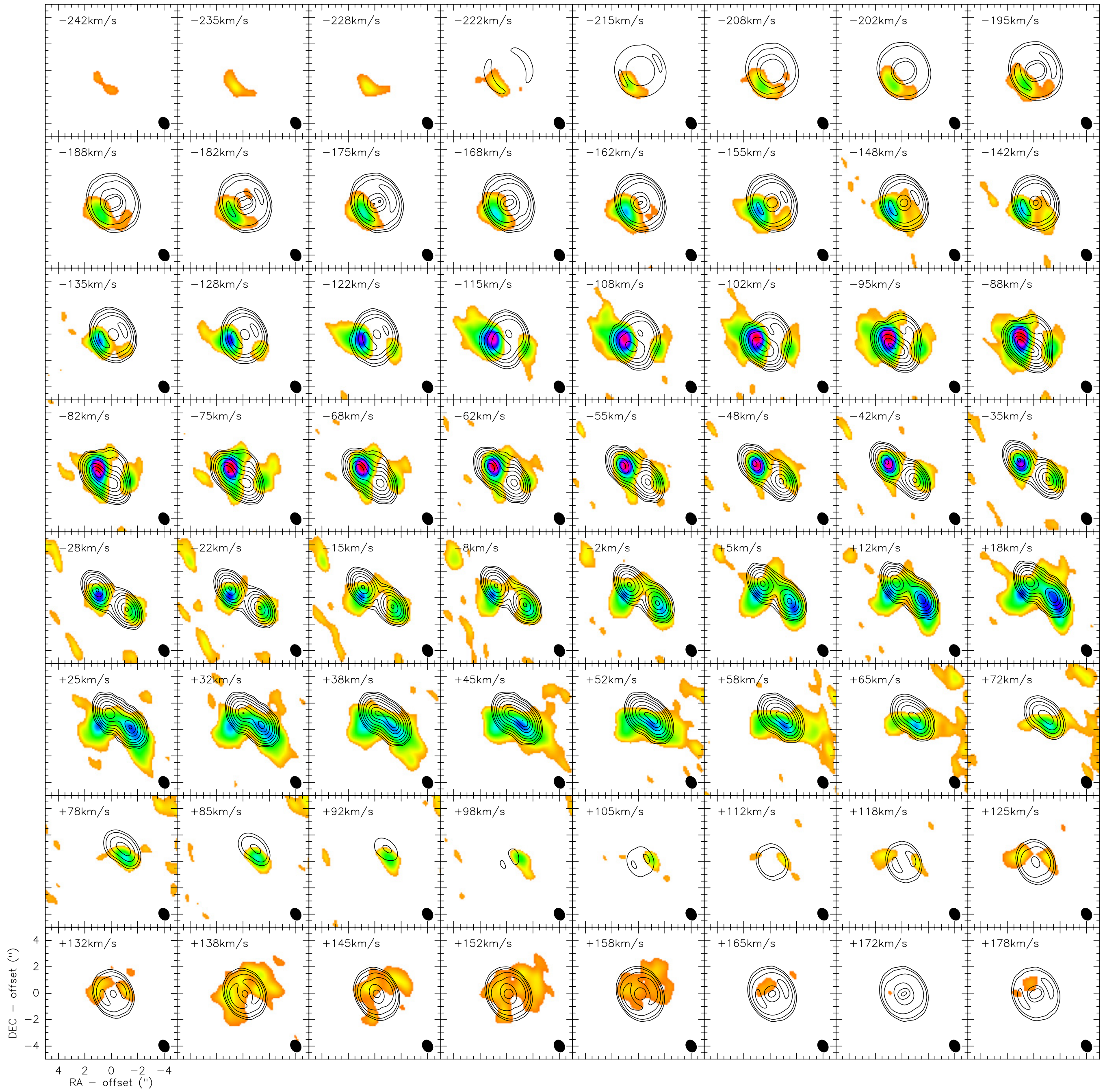

Figure 16. Velocity channel maps of the CO model compared to the ^{12}CO(2–1) emission.
(A color version of this figure is available in the online journal.)

starbursting regions ($X^{\mathrm{HCN,g}}_{\mathrm{HCO^+}} \simeq 1$). However, good solutions are also found for lower kinetic temperatures. This is due to the fact that HCN and HCO$^+$ are not as sensitive to changes in the kinetic temperatures as ^{12}CO and ^{13}CO. They are better indicators of changes in the volume density, as can be seen in Figure 22; the volume density is restricted by the χ^2 test to a very small area and independently yields values of $n(\mathrm{H_2}) \simeq 10^{3.5}$–$10^{4.5}$ cm^{-3} similar to the ^{12}CO and ^{13}CO results.

The simulations[17] indicate column densities for HCN in the range $N(\mathrm{HCN}) \simeq 10^{12.0}$–$10^{13.5}$ cm^{-2}, which is smaller (by a factor of ∼10) than what was found by Krips et al. (2008) with the LVG code. However, results are quite similar to Krips et al. (2008) when assuming similar kinetic temperatures.

Comparing the HCN column densities to those of ^{12}CO ($N(^{12}\mathrm{CO}) \simeq 10^{17.0}$–$10^{19.0}$ cm^{-2}), we obtain abundance ratios between HCN and ^{12}CO of $X^{^{12}\mathrm{CO}}_{\mathrm{HCN}} \gtrsim 10^{3.5}$, which still seems to be compatible with a slightly increased abundance of HCN. Comparing the column densities of HCO$^+$ and ^{12}CO, we find a somewhat decreased HCO$^+$ abundance (by a factor of at least 10 lower than that found in Galactic star-forming regions). This agrees well with previous results (e.g., García-Burillo et al. 2010; Krips et al. 2008; Usero et al. 2004), suggesting an

[17] Note that we consider the two highest contours in Figure 22 as being acceptable solutions.

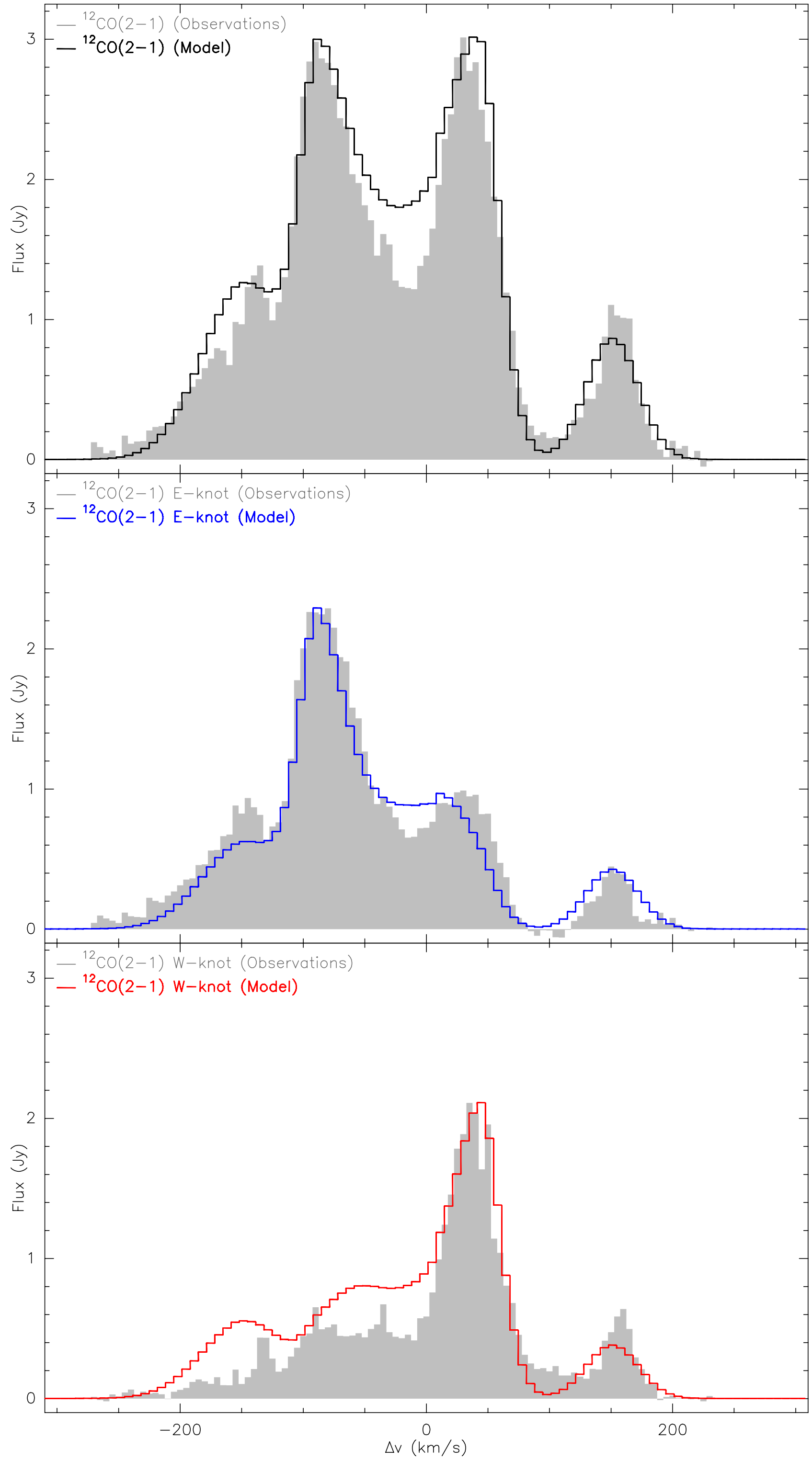

Figure 17. Spectrum of the CO model compared to the ^{12}CO(2–1) emission.
(A color version of this figure is available in the online journal.)

increased formation (and hence increased abundance) of HCN due to an XDR in the center of NGC 1068.

6. SUMMARY AND CONCLUSIONS

The SMA and PdBI observations of the (sub)millimeter emission in NGC 1068 presented in this paper show complex distribution, kinematics, and excitation conditions of the molecular gas. The (sub)millimeter continuum and molecular line emission is interpreted as follows.

1. The centimeter/millimeter continuum emission seems to be best reproduced by electron-scattered synchrotron emission. Thermal free–free emission as proposed by Hönig et al. (2008) overpredicts the high angular resolution 1 mm continuum emission.

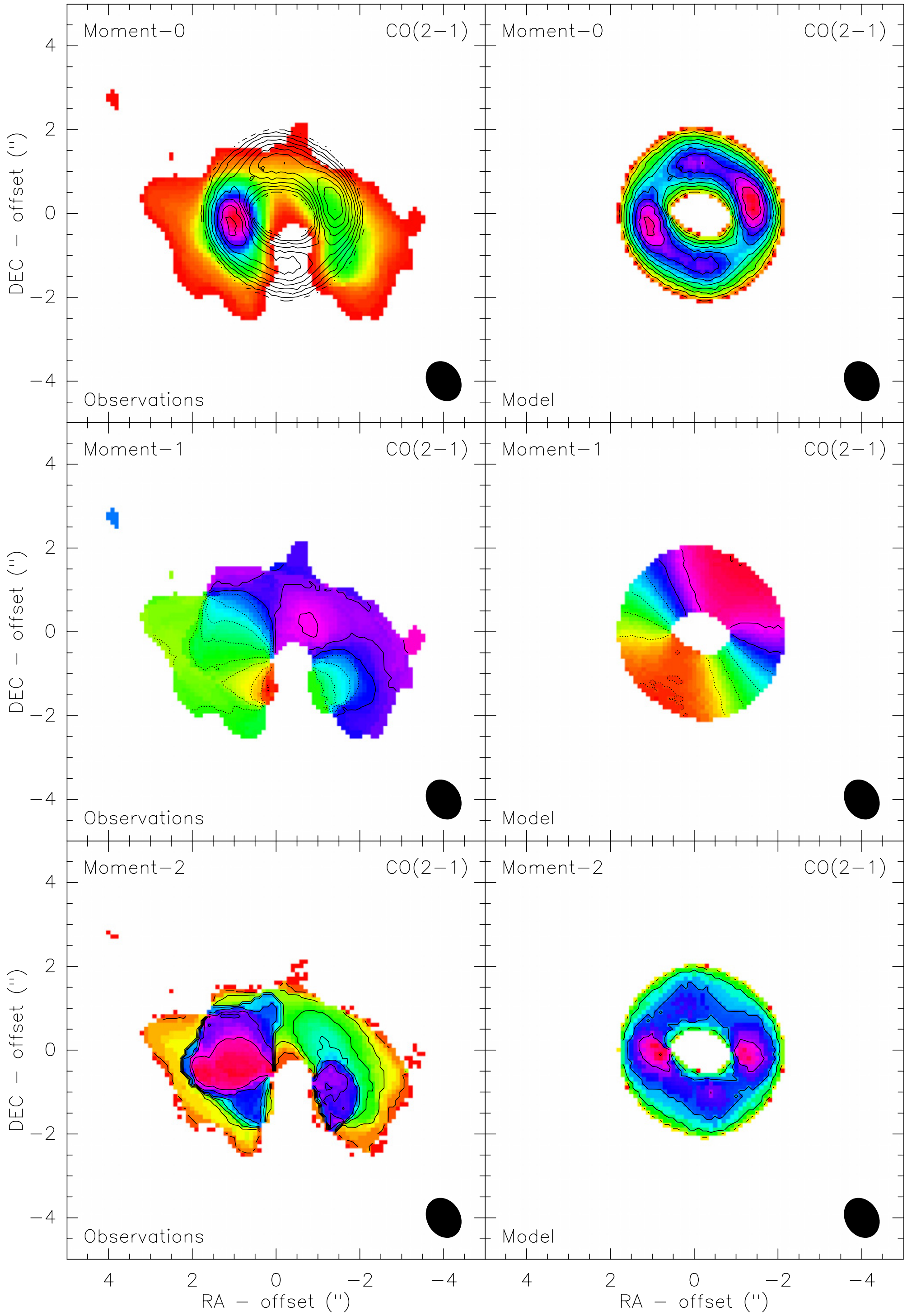

Figure 18. Moment maps of the CO model compared to the ^{12}CO(2–1) emission. The velocities are plotted in steps of 20 km s^{-1} for the Moment 1 and Moment 2 maps.

(A color version of this figure is available in the online journal.)

2. The molecular gas is found to display a very complex kinematic behavior in the ^{12}CO, HCN, and HCO$^+$ lines, which is not reproducible by a tilted-ring model approximating a warped disk with circular motions. Instead, a dominant rotating disk plus a radial outflow of some of the gas in the CND is proposed as an alternative explanation to account for the non-circular motions.
3. The different line ratios from the ^{12}CO, ^{13}CO, HCN, and HCO$^+$ emission seem to be consistent with moderately dense and warm gas, lending further support to a gas scenario heated and compressed by a shock (at least in the north/northeastern part of the ring). The highest line ratios are found close to the AGN and/or jet–CND "contact" point. In this picture, the increased kinetic temperatures

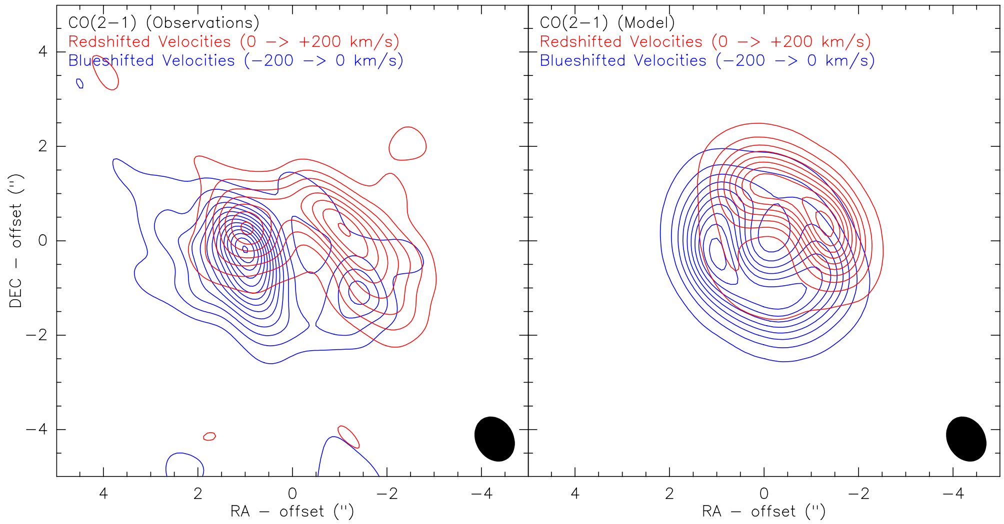

Figure 19. Blueshifted and redshifted emission of the CO model compared to the ^{12}CO(2–1) emission.
(A color version of this figure is available in the online journal.)

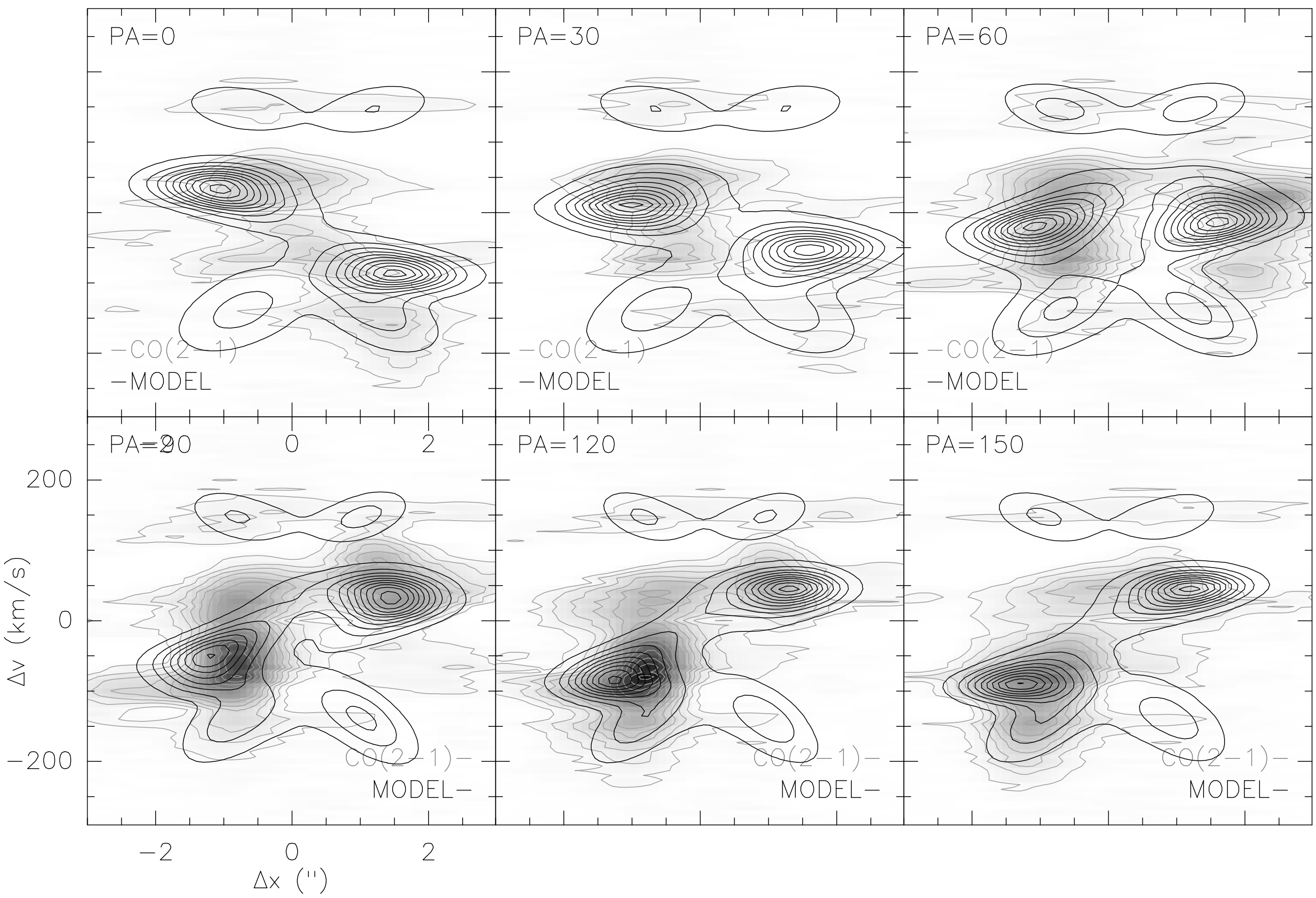

Figure 20. Position–velocity diagram of the CO model compared to the ^{12}CO(2–1) emission.

seem to be one of the culprits for the unusually high HCN-to-CO($J = 1$–0) line ratios due to a hypo-excitation of the CO($J = 1$–0) line emission.

4. Consistent with previous papers, we find further indications of an increased HCN abundance in NGC 1068 (by a factor of ∼4–10), and a decreased HCO$^+$ abundance (by a factor of ∼5–10), explaining the high HCN-to-HCO$^+$ abundance ratio in the CND of this source.

The Submillimeter Array is a joint project between the Smithsonian Astrophysical Observatory and the Academia Sinica Institute of Astronomy and Astrophysics and is funded by the Smithsonian Institution and the Academia Sinica. We thank the anonymous referee for a very careful and constructive report. We also thank Gaelle Dumas for a very useful discussion on and help with the kinematic analysis of the ^{12}CO data. I.S. acknowledges grant LC06014 of the Ministry of Education of the

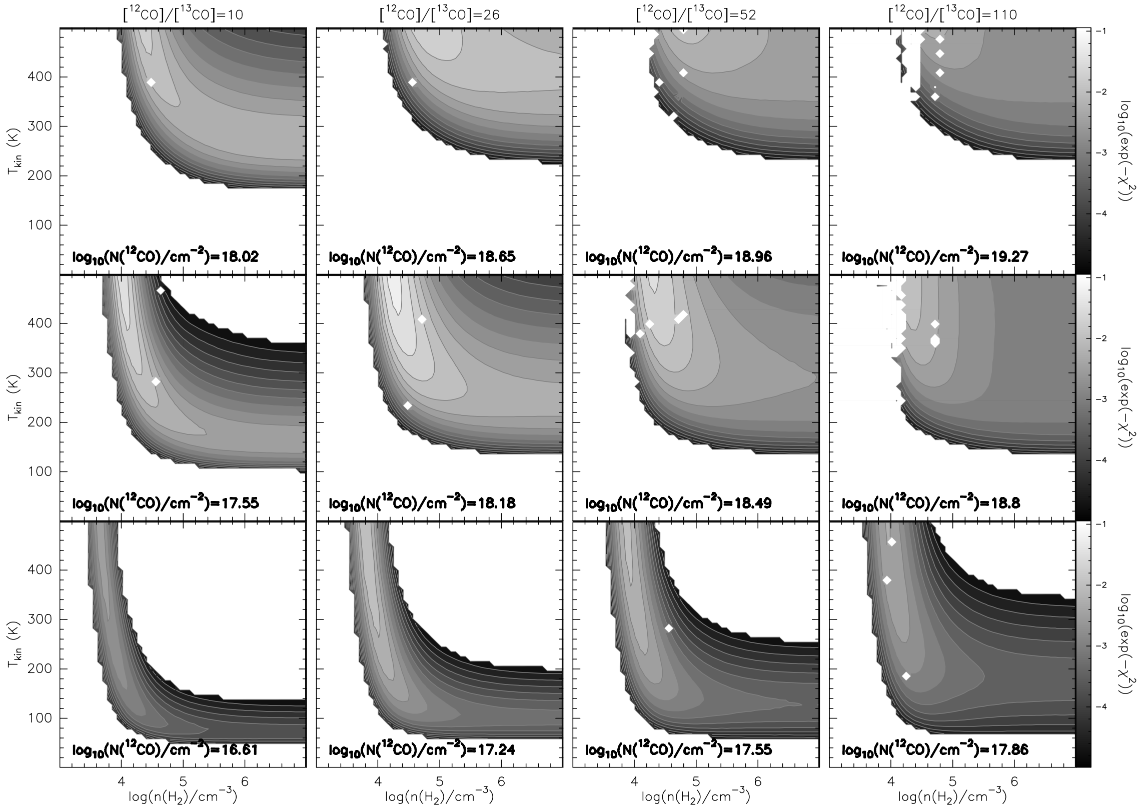

Figure 21. χ^2 fit results obtained from the RADEX simulations of the excitation conditions of the molecular gas. Four different [^{12}CO]/[^{13}CO] abundance ratios (= 10, 26, 52, and 110) for three different ^{12}CO column densities are shown. The middle panel shows the best χ^2 fit found for each abundance ratio.

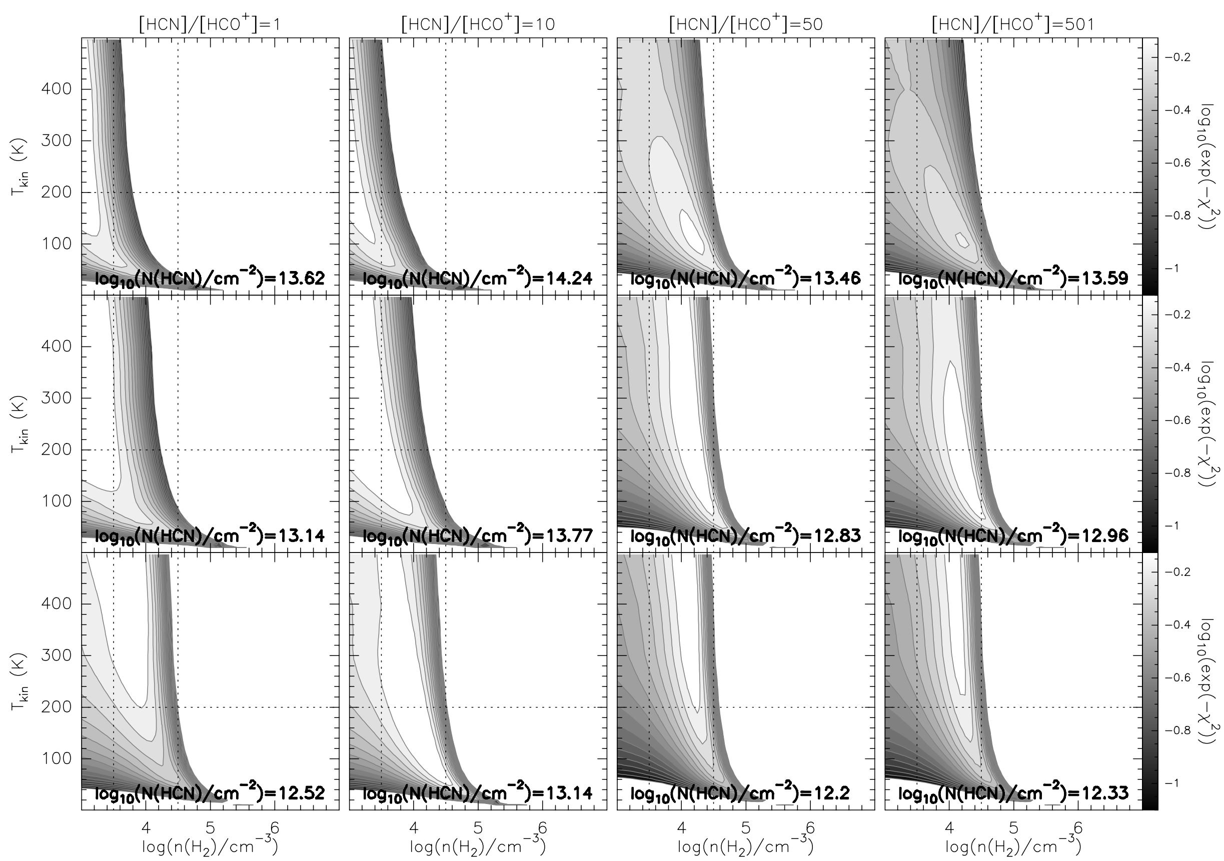

Figure 22. χ^2-fit results obtained from the RADEX simulations of the excitation conditions of the molecular gas. Four different [HCN]/[HCO$^+$] abundance ratios around the standard Galactic value of [HCN]/[HCO$^+$] $\simeq$ 10 for three different HCN column densities are shown. The middle panel shows the best χ^2 fit found for each abundance ratio.

Czech Republic. A.B.P. thanks the National Radio Astronomy Observatory (NRAO) for support on this project. NRAO is a facility of the National Science Foundation operated under cooperative agreement by Associated Universities, Inc. S.M. is supported by the National Science Council (NSC) of Taiwan, NSC 97-2112-M-001-021-MY3.

REFERENCES

Aalto, S. 2008, Ap&SS, 313, 273
Antonucci, R. R. J., & Miller, J. S. 1985, ApJ, 297, 621
Ao, Y., Henkel, C., Braatz, J. A., Wei, A., Menten, K. M., & Mhle, S. 2011, A&A, 529, 154
Baum, S. A., Heckman, T. M., & van Breugel, W. 1992, ApJ, 389, 208
Blake, G. A., Sutton, E. C., Masson, C. R., & Phillips, T. G. 1987, ApJ, 315, 621
Bland-Hawthorn, J., Gallimore, J. F., Tacconi, L. J., Brinks, E., Baum, S. A., Antonucci, R. R. J., & Cecil, G. N. 1997, Ap&SS, 248, 9
Bock, J. J., et al. 2000, AJ, 120, 2904
Cotton, W. D., Jaffe, W., Perrin, G., & Woillez, J. 2008, A&A, 477, 517
Dale, D. A., Sheth, K., Helou, G., Regan, M. W., & Hüttemeister, S. 2005, AJ, 129, 2197
Fuente, A., García-Burillo, S., Gerin, M., Teyssier, D., Usero, A., Rizzo, J. R., & de Vicente, P. 2005, ApJ, 619, L155
Galliano, E., & Alloin, D. 2002, A&A, 393, 43
Galliano, E., Pantin, E., Alloin, D., & Lagage, P. O. 2005, MNRAS, 363, L1
Gallimore, J. F., Baum, S. A., & O'Dea, C. P. 1996, ApJ, 464, 198
Gallimore, J. F., Baum, S. A., & O'Dea, C. P. 2004, ApJ, 613, 794
Gallimore, J. F., Henkel, C., Baum, S. A., Glass, I. S., Claussen, M. J., Prieto, M. A., & von Kapherr, A. 2001, ApJ, 556, 694
Gao, Y., & Solomon, P. M. 2004, ApJ, 606, 271
García-Burillo, S., Combes, F., Usero, A., & Graciá-Carpio, J. 2007, New Astron. Rev., 51, 160
García-Burillo, S., Combes, F., Usero, A., & Graciá-Carpio, J. 2008, J. Phys. Conf. Ser., 131, 2031
García-Burillo, S., et al. 2010, A&A, 519, 2
Greenhill, L. J., Gwinn, C. R., Antonucci, R., & Barvainis, R. 1996, ApJ, 472, L21
Greve, T. R., Papadopoulos, P. P., Gao, Y., & Radford, S. J. E. 2009, ApJ, 692, 1432
Guilloteau, S., & Lucas, R. 2000, in Imaging at Radio Through Submillimeter Wavelengths, ed. J. G. Mangum & S. J. E. Radford (San Francisco, CA: ASP), 299
Heckman, T. M., Baum, S. A., van Breugel, W. J. M., & McCarthy, P. 1989, ApJ, 338, 48
Henkel, C., Chin, Y.-N., Mauersberger, R., & Whiteoak, J. B. 1998, A&A, 329, 443
Henkel, C., Downes, D., Weiß, A., Riechers, D., & Walter, F. 2010, A&A, 516, 111
Henkel, C., & Mauersberger, R. 1993, A&A, 274, 730
Henkel, C., Mauersberger, R., Wiklind, T., Huettemeister, S., Lemme, C., & Millar, T. J. 1993, A&A, 268, L17
Henkel, C., Whiteoak, J. B., & Mauersberger, R. 1994, A&A, 284, 17
Hönig, S. F., Almudena Prieto, M., & Beckert, Th. 2008, A&A, 485, 33
Huchra, J. P., Vogeley, M. S., & Geller, M. J. 1999, ApJS, 121, 287
Humphreys, E. M. L., Greenhill, L. J., Reid, M. J., Beuther, H., Moran, J. M., Gurwell, M., Wilner, D. J., & Kondratko, P. T. 2005, ApJ, 634, L133
Irvine, W. M., Goldsmith, P. F., & Hjalmarson, A. 1987, in Proc. Symp., Interstellar Processes, ed. D. J. Hollenbach & H. A. Thronson (Dordrecht: Reidel), 561
Israel, F. P. 2009, A&A, 493, 525
Jaffe, W., et al. 2004, Nature, 429, 47
Kamenetzky, J., et al. 2011, ApJ, 731, 83
Khachikian, E. Y., & Weedman, D. W. 1974, ApJ, 192, 581
Kohno, K., Kawabe, R., Tosaki, T., & Okumura, S. 1996, ApJ, 461, L29
Kohno, K., Matsushita, S., Vila-Vilaró, B., Okumura, S. K., Shibatsuka, T., Okiura, M., Ishizuki, S., & Kawabe, R. 2001, in ASP Conf. Ser. 249, The Central kpc of Starbursts and AGN, ed. J. H. Knapen et al. (San Francisco, CA: ASP), 672
Kohno, K., Nakanishi, K., Tosaki, T., Muraoka, K., Miura, R., Ezawa, H., & Kawabe, R. 2008, Ap&SS, 313, 279
Kraemer, S. B., Ruiz, J. R., & Crenshaw, D. M. 1998, ApJ, 508, 232
Krips, M., Martín, S., Neri, R., García-Burillo, S., Combes, F., Petitpas, G., Fuente, A., & Usero, A. 2009, in ASP Conf. Ser. 408, The Starburst–AGN Connection, ed. W. Wang et al. (San Francisco, CA: ASP), 142
Krips, M., Neri, R., García-Burillo, S., Martín, S., Combes, F., Graciá-Carpio, J., & Eckart, A. 2008, ApJ, 677, 262
Krips, M., et al. 2006, A&A, 446, 113
Krips, M., et al. 2007, A&A, 468, L63
Krolik, J. H., & Kallman, T. R. 1987, ApJ, 320, L5
Martín, S., Aladro, R., Martín-Pintado, J., & Mauersberger, R. 2010, A&A, 522, 62
Martín, S., Mauersberger, R., Martín-Pintado, J., Henkel, C., & García-Burillo, S. 2006, ApJS, 164, 450
Martín, S., et al. 2011, A&A, 527, 36
Matsushita, S., Kawabe, R., Kohno, K., Matsumoto, H., Tsuru, T. G., & Vila-Vilaró, B. 2005, ApJ, 618, 712
Matsushita, S., Kawabe, R., Matsumoto, H., Tsuru, T. G., Kohno, K., Morita, K.-I., Okumura, S. K., & Vila-Vilaró, B. 2000, ApJ, 545, L107
Matsushita, S., Kohno, K., Vila-Vilaró, B., Tosaki, T., & Kawabe, R. 1998, ApJ, 495, 267
Matsushita, S., Muller, S., & Lim, J. 2007, A&A, 468, L49
Matsushita, S., et al. 2004, ApJ, 616, L55
Meier, D. S., & Turner, J. L. 2005, ApJ, 618, 259
Meijerink, R., & Spaans, M. 2005, A&A, 436, 397
Meijerink, R., Spaans, M., & Israel, F. P. 2007, A&A, 461, 793
Muller, S., Guelin, M., Dumke, M., Lucas, R., & Combes, F. 2006, A&A, 458, 417
Müller-Sànchez, F., Davies, R. I., Genzel, R., Tacconi, L. Jz., Eisenhauer, F., Hicks, E. K. S., Friedrich, S., & Sternberg, A. 2009, ApJ, 691, 749
Naylor, B. J., et al. 2010, ApJ, 722, 668
Papadopoulos, P. P. 2010, ApJ, 720, 226
Pérez-Beaupuits, J. P., Spaans, M., van der Tak, F. F. S., Aalto, S., García-Burillo, S., Fuente, A., & Usero, A. 2009, A&A, 503, 459
Poncelet, A., Perrin, G., & Sol, H. 2008, A&A, 481, 305
Rigopoulou, D., Kunze, D., Lutz, D., Genzel, R., & Moorwood, A. F. M. 2002, A&A, 389, 374
Roussel, H., et al. 2007, ApJ, 669, 959
Roy, A. L., Colbert, E. J. M., Wilson, A. S., & Ulvestad, J. S. 1998, ApJ, 504, 147
Sakamoto, K., Aalto, S., Evans, A. S., Wiedner, M. C., & Wilner, D. J. 2010, ApJ, 725, L228
Sakamoto, K., Ho, P. T. P., & Peck, A. B. 2006, ApJ, 644, 862
Schinnerer, E., Eckart, A., Tacconi, L. J., Genzel, R., & Downes, D. 2000, ApJ, 533, 850
Scoville, N. Z., Carlstrom, J. E., Chandler, C. J., Phillips, J. A., Scott, S. L., Tilanus, R. P. J., & Wang, Z. 1993, PASP, 105, 1482
Siemiginowska, A., & Elvis, M. 1997, ApJ, 482, L9
Sternberg, A., Genzel, R., & Tacconi, L. 1994, ApJ, 436, L131
Tacconi, L. J., Genzel, R., Blietz, M., Cameron, M., Harris, A. I., & Madden, S. 1994, ApJ, 426, L77
Tomono, D., Terada, H., & Kobayashi, N. 2006, ApJ, 646, 774
Usero, A., García-Burillo, S., Fuente, A., Martín-Pintado, J., & Rodríguez-Fernàndez, N. J. 2004, A&A, 419, 897
Usero, A., García-Burillo, S., Martín-Pintado, J., Fuente, A., & Neri, R. 2006, A&A, 448, 457
Van der Tak, F. F. S., Black, J. H., Schöier, F. L., Jansen, D. J., & van Dishoeck, E. F. 2007, A&A, 468, 627
Wang, M., Henkel, C., Chin, Y.-N., Whiteoak, J. B., Hunt, C. M., Mauersberger, R., & Muders, D. 2004, A&A, 422, 883
Wilson, T. L., & Matteucci, F. 1992, A&AR, 4, 1
Wilson, T. L., & Rood, R. 1994, ARA&A, 32, 191